TÉCNICO LISBOA

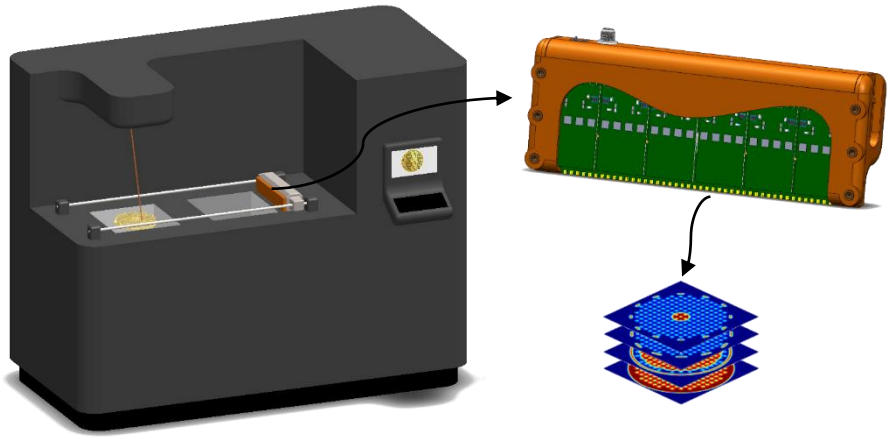

Scalable Coil Sensors Readout for Eddy Current Testing Array Probes

Pedro Gonçalo da Silva Faria

Thesis to obtain the Master of Science Degree in

Electronics Engineering

Supervisor: Prof. Luís Filipe Soldado Granadeiro Rosado

Examination Committee

Chairperson: Prof. Paulo Ferreira Godinho Flores

Supervisor: Prof. Luís Filipe Soldado Granadeiro Rosado

Member of the Committee: Prof. Diogo Miguel Bárbara Coroas Prista Caetano

October 2023

Declaration

I declare that this document is an original work of my own authorship and that it fulfills all the requirements of the Code of Conduct and Good Practices of the Universidade de Lisboa.

Declaração

Declaro que o presente documento é um trabalho original da minha autoria e que cumpre todos os requisitos do Código de Conduta e Boas Práticas da Universidade de Lisboa.

Acknowledgments

First and foremost, I would like to express my deepest gratitude to my supervisor, Luís Rosado, for the invaluable guidance, unwavering support, and endless patience throughout the entire development process. His expertise and encouragement played a significant role in shaping this thesis.

I am profoundly thankful to André Barrancos for his invaluable assistance and our enthusiastic discussions. I am also grateful for his initial probe design that laid the foundation for this work.

I am incredibly thankful to the Instituto de Soldadura e Qualidade (ISQ), specifically to Dr. Rodolfo Batalha, whose efforts made the production of Powder Bed Fusion specimens possible, thereby elevating my thesis to a higher level.

I would like to thank Instituto de Telecomunicações - Grupo de Instrumentação e Medidas for all the support provided as well as the EMLAYERING project - EXPL/EEI-EEE/0394/2021 funded by Fundação para a Ciência e a Tecnologia (FCT). Additionally, I appreciate the assistance provided by the Departamento de Engenharia Eletrótecnica e de Computadores – Área Científica de Eletrónica for granting me access to their facilities.

I am profoundly thankful to my parents, Inácio and Zélia, and my sister, Carolina, for their constant love and encouragement. Their belief in me has been my driving force, and I am truly blessed to have them by my side.

I am profoundly grateful to my girlfriend, Leonor, for her love, support, and understanding. Her presence has been my source of strength, and I am truly fortunate to have her in my life.

I sincerely appreciate my friends for their understanding, encouragement, and occasional distractions that helped me maintain my sanity during the stressful academic journey. I want to especially thank my dear friend Jorge Antunes for his valuable advice and support during the best and worst moments.

Lastly, I express my gratitude to all those who supported me in various ways, regardless of how big or small their contributions may have been. Your kindness and assistance have not gone unnoticed, and I am genuinely appreciative of the help I received.

Abstract

In recent years, Additive Manufacturing (AM) technology has revolutionized the production of metal objects. The Powder Bed Fusion (PBF) is one of the most popular production technologies. However, the inherent process variability demands higher robustness to prevent defects such as pores, surface roughness, and delamination. Rigorous industry and certification requirements make Quality Control (QC) mandatory. Although postproduction QC methods are widely available, the demand for in-situ monitoring systems to produce ready-for-use parts using real-time feedback is rising. In recent years, Eddy Current Testing has been pointed out as a candidate method to effectively QC. This electromagnetic method allows the characterization of surface and near-surface defects, making it ideal for layer-by-layer QC of metal objects during fabrication.

This thesis presents an advanced Eddy Current Probe (ECP) array tailored for layer-by-layer QC metal parts produced using PBF. The probe operates mounted on the PBF printer recoater, allowing layer-wise imaging to entirely reconstruct the metal part under production. The enhanced design for stimulation and acquisition allows a spatial resolution of 1 mm and a sampling frequency of 31.25 kHz. The layer-wise scan approach eliminates the need for high penetration, leading to a stimulation frequency of 1 MHz. Moreover, the probe incorporates a sensor array featuring 240 coils for scanning wider metal areas aligning with the typical dimensions of the powder beds. The system successfully exhibits capabilities to scan PBF parts, achieving scan resolutions as low as 0.16 mm at 250 mm/s speeds.

Keywords: Additive Manufacturing, Eddy Current Testing, Powder Bed Fusion, Synchronous Demodulation & Sampling, Embedded Systems.

Resumo

Nos últimos anos a tecnologia de fabrico aditivo revolucionou a produção de objetos metálicos. A Fusão Seletiva em Camada de Pó (FSCP) é uma das tecnologias mais populares. No entanto, a variabilidade inerente ao processo exige uma maior robustez para prevenir defeitos como poros, rugosidades superficiais e delaminação. Os requisitos e a certificação rígida tornam o Controlo de Qualidade (CQ) obrigatório. Embora o CQ pós-produção estar amplamente disponível, a procura por sistemas de monitorização locais para produzir peças prontas para utilização, com controlo em tempo real, está a aumentar. Nos últimos anos, o teste com correntes induzidas tem sido apontado como um método eficaz para CQ. Este método eletromagnético permite a caracterização de defeitos superficiais e próximos à superfície, tornando-o ideal para CQ, camada a camada, de objetos metálicos durante a fabricação.

Esta tese apresenta uma sonda matricial avançada projetada para CQ camada a camada de peças metálicas produzidas com FSCP. A sonda opera montada no espalhador de pó da impressora de FSCP, permitindo a imagiologia por camadas para reconstruir a peça metálica na sua totalidade. O desenho otimizado da estimulação e aquisição permite uma resolução espacial de 1 mm e uma frequência de amostragem de 31.25 kHz. A imagiologia por camadas elimina a necessidade de uma penetração elevada, resultando numa frequência de estimulação de 1 MHz. Além disso, a sonda possui 240 bobines para mapear regiões metálicas alargadas, alinhando-se com as dimensões típicas das bases de produção. O sistema demonstrou com sucesso capacidades para mapear peças de FSCP, atingindo imagens com resoluções de 0.16 mm com velocidades de 250 mm/s.

Palavras-chave: Fabrico aditivo, Teste de Correntes Induzidas, Fusão Seletiva em Camada de Pó, Desmodulação e Amostragem Síncrona, Sistemas embebidos.

Contents

List of Figures

List of Tables

Acronyms

AC ..... Alternating Current
ADC ..... Analog to Digital Conversion
AFE ..... Analog Front End
ASTM ..... American Society for Testing and Materials
BPF ..... Band-Pass Filter
BRAM ..... Block Random Access Memory
BS ..... British Standards
CNC ..... Computer Numerical Control
DAC ..... Digital to Analog Converter
DDS ..... Direct Digital Synthesis
DMA ..... Direct Memory Access
EB-PBF ..... Electron Beam PBF
EC ..... Eddy Current
ECPI ..... Eddy Current Probes Interface
ECT ..... Eddy Current Testing
ENOB ..... Effective Number of Bits
FEA ..... Finite Element Analysis
FSR ..... Full-Scale Range
GAP ..... Generic Access Profile
GATT ..... Generic Attribute
HF ..... High Frequency
HPF ..... High-Pass Filter
ICI ..... In-line Coherent Imaging
IP. ..... Intellectual Property
ISO ..... International Organization for Standardization
ISQ ..... Instituto de Soldadura e Qualidade
LB-PBF ..... Laser Beam PBF
LF ..... Low-Frequency
LPF ..... Low-Pass Filter
LwIP ..... Lightweight IP
LWIR ..... Long Wave Infrared
MAF ..... Moving Average Filter
MR ..... Magneto-Resistive
NDT ..... Non-Destructive Testing
OPAMP ..... Operational Amplifier
OSR ..... Oversampling Ratio
PBF ..... Powder Bed Fusion
PL ..... Programmable Logic
PLL ..... Phase-Locked-Loop
PS ..... Processing System
QC ..... Quality Control
S&H ..... Sample & Hold
SAR ..... Successive Approximation Register
SCM ..... Stimulation Coil Module
SD ..... Secure Digital
SDK ..... Software Development Kit
SDS ..... Synchronous Demodulation & Sampling
SNR ..... Signal-to-Noise Ratio
SoC ..... System on Chip
SPI ..... Serial Peripheral Interface
SPP ..... Serial Port Profile
SRAS ..... Spatially Resolved Acoustic Spectroscopy
SYNC ..... Synchronism
WECAP ..... Wireless Eddy Current Array Prototype

1. Introduction

1.1 Purpose and Motivation

Additive Manufacturing (AM) of metallic objects is a technology that has earned tremendous popularity across several manufacturing sectors. Among others, medical, aerospace, automobile, and military are some predominant fields adopting the process [1]. The concept relies on “joining materials to make objects from a 3D model data, usually layer upon layer” [2]. It enables the production of complex geometries and shapes, providing unprecedented design flexibility [3].

The Powder Bed Fusion (PBF) is the industry’s most used form of metal AM due to its superior capability of making geometrically complex parts [1]. Aerospace frequently uses it to reduce component weight, lead times, and costs, such as in NASA, to produce rocket injectors [4]. The process relies on the layer-wise melting of a powder bed using a laser. It is a conceptually simple process, but the high heating and cooling rates it often results in objects with a rough surface and significant porosity [1].

The absence of a robust PBF process is one of the main barriers to the broader adoption of AM [3]. The recent interest in using PBF is increasing the need for Quality Control (QC) [5] to overcome the process's inherent variability. There is a constant demand to maximize the part quality and consistency to obtain ready-for-use parts within the industry requirements [3], [4]. For this reason, in-situ monitoring is vital for the technology to mature by identifying and understanding defective conditions. It allows real-time control of the process parameters while manufacturing, enhancing the final piece's reliability.

Eddy Current Testing (ECT) is a well-established Non-Destructive Testing (NDT) technique used frequently for QC inspection in post-production scenarios. It is a contactless electromagnetic method inducing and sensing electrical current on conductive materials. The method allows for measuring material properties like conductivity and supports detecting and characterizing surface and near-surface defects (e.g., porosity, cracks). The characteristics are suitable for integration into a layer-wise QC in-situ system able to provide the information of entire produced metal pieces with PBF. A few cases have emerged in recent years showing the ability to use it in such a context.

This work resulted in a new one-dimensional Eddy Current Probe (ECP) array specifically designed to mount directly on the recoater within the PBF 3D printer, as illustrated in Figure 1.1.1.

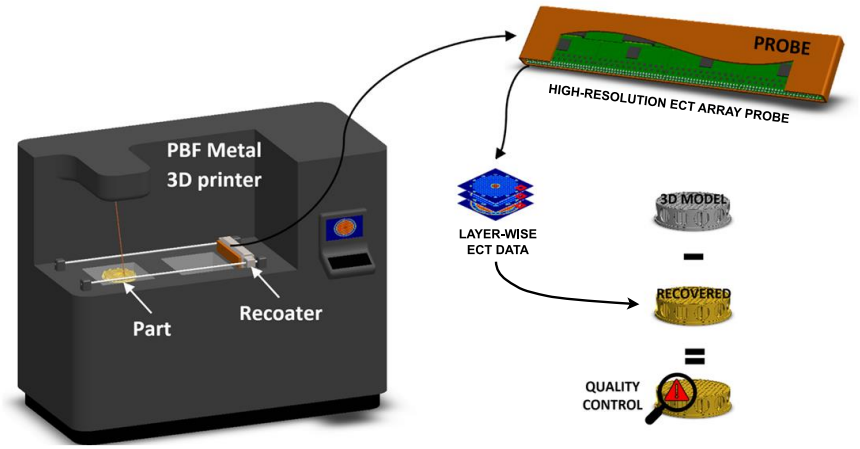

Figure 1.1.1: ECT array setup goal for a PBF AM 3D printer, adapted from [6].

The presented setup allows performing layer-wise imaging. The probe scans the metal part each time the recoater moves to distribute the powder over the build platform. Meanwhile, as the recoater returns

to its initial position and the laser melts the necessary regions, the probe transmits the material integrity data to the host computer to build and store the layer ECT scans. Upon completion of the metal part production, the host computer can reconstruct the entire specimen. This reconstruction will one day allow the printer technician to QC (inspect) the specimen compared with the 3D model.

This thesis presents the development of the system until the layer ECT scans storage, including essential studies regarding its geometry and operation. The probe takes advantage of the constant stimulation independent of the specimen properties and the sensing coils' position to enhance the sensitivity. The main improvements over the previously available probes include an enhanced spatial resolution allowing adequate characterization in a single recoater pass and high acquisition frequency, ensuring high scan resolution without constraining the recoater speed. Additionally, the probe incorporates a minimal signal demodulation circuitry, reducing temperature dependencies and channel mismatch. The encouraging results in a prototype version led to the design of a probe with an array length capable of scanning most of the powder bed sizes in the industry.

1.2 Goals and Challenges

The goal of this project is to develop an ECP array to operate in a layer-wise monitoring scenario. The system acquires the material integrity data, providing the layers imaging results. This capability allows the full part reconstruction, enabling companies to study the manufacturing process and reduce post-production processes. To develop this equipment successfully, the tasks below are necessary:

- Design and prototype an Eddy Current (EC) stimulation module capable of driving inductive loads with high and constant amplitude alternate currents.
- Study new possibilities for minimal signal demodulation to read out the ECP array sensor coils.
- Build and prototype a new ECP array using an independent sensing and stimulation approach.
- Evaluate and implement a method for integrating several ECPs for higher scanning areas.

Developing an ECT probe for scanning the PBF production process presents several challenges considering the printer operation and the desired layer characterization level, including:

- High sampling frequency with parallel readout.
- Wide sensor array with high spatial resolution.
- Wireless, compact, and light probe.

The outlined features ensure the ECT probe integrates with the metal printer, maintaining regular operation without limitations. Fast readout is crucial for achieving a high scan resolution without recoater slowdown (up to 250 mm/s). It demands a digital core for parallel data retrieval at high throughput, bypassing delays linked to traditional multiplex approaches.

Multiple sensors within the array are essential for full platform coverage (up to 600 mm [7]), requiring the digital core to manage substantial high-frequency data. A low sensor pitch enables single-pass acquisition of necessary data for layer characterization, but consideration is needed to control the sensitivity impact on electronic circuitry and sensors.

Finally, the probe must be wireless, compact, and light to limit the modifications inside the printer chamber to a single bracket and avoid mechanical stress on the recoater.

1.3 Document Organization

This document is divided into four chapters, as follows:

- Chapter 2 provides the reader with the essential background information, an overview of ECT, explaining the physical principles, standard acquisition methods, and information around the application PBF AM. This chapter also explores the state-of-the-art on this topic.
- Chapter 3 presents the preliminary version of the ECP prototype. The chapter focuses on the hardware, firmware, and software developed. It offers in-depth explanations and design decisions throughout development and concludes by showing the dedicated demonstrator.
- Chapter 4 introduces the latest ECP equipment developed. It starts with the improvements performed addressing the previous versions' hardware limitations. The emphasis of this chapter is on the implementation of the new digital component.
- Chapter 5 presents the results over generic patterns and imaging results from PBF parts.
- Chapter 6 presents an overview of the entire thesis, conclusions drawn from the equipment performance, and future work.

1.4 Contributions

During the development of this thesis, the author collaborated with the Instituto de Telecomunicações – Grupo de Instrumentação e Medidas research group. This association supported the completion of this thesis but also offered the opportunity to be involved and assist bachelor students in their final year projects, the 1ST Cycle Integrated Project in Electronics Engineering. Some notable projects contributed to include:

- P. Carvalho, T. Fernandes, "Breakout Board Design and Characterization of a Programmable Alternating Current Source, PIC1 Project, Instituto Superior Técnico", 2023
- G. Cecílio, J. Silva, "Demonstrating an Eddy Current Displacement Sensors Array in a Non-Mechanized Gas Pedal, PIC1 Project, Instituto Superior Técnico", 2023

Additionally, the author was responsible for developing a dedicated LabView software, elaborated further in this document, designed to integrate any inspection probe. This software facilitated the thesis and is a valuable resource for future students and researchers.

2. Background

2.1 Eddy Current Testing

In the metal industry and science, the quality control of the materials usually leans over NDTs. These evaluate a wide variety of materials without causing damage. Electromagnetic, ultrasonic, and die penetrant testing are some of the most popular techniques.

ECT is one of the electromagnetic techniques of NDT. This method inspects electrically conductive materials at very high speeds without direct physical contact. It allows crack detection in several conductive materials, such as ferromagnetic or non-ferromagnetic metals [8]. This section discusses the principles, considerations, and methods required when developing an ECT system.

2.1.1 Physical principle

The ECT physical principle relies on the interaction between a magnetic field and the material under test. The procedure starts with a coil energized with an Alternating Current (AC) signal to create a primary magnetic field. Then, approaching the coil into the material causes its magnetic field to penetrate, inducing continuous and circular ECs in the material. These will generate a secondary magnetic field opposing the primary. The eddy currents will be affected in case of changes in conductivity, near-surface defects (cracks), or differences in thickness. The sensing coil impedance decreases according to the increased eddy current intensity [8]. So, measuring the coil impedance variation allows the sense of the EC and tracking the material modifications. The current or voltage signal is measured to monitor the impedance. This coil can be the same or a sense-dedicated one. Figure 2.1.1 shows a representation of the physical principle.

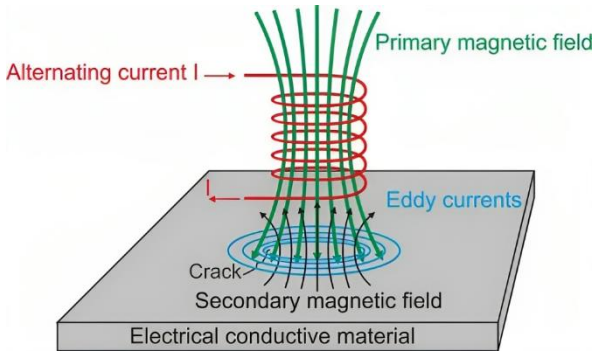

Figure 2.1.1: Eddy current physical principle in [8].

According to Ampere-Maxwell [9] and Faraday's [10] equations, it is possible to obtain a more detailed overview of the physical principle. Considering an alternating current I_L flowing through a coil L in a perpendicular surface S, the magnetic field $\vec{H}$, the intensity of the lines is

$$\oint_S \vec{H}\, d\vec{l} = \mu_0 I_L + \mu_0 \epsilon_0 \frac{d\phi_E}{dt}, \tag{2.1.1}$$

where μ_0 is the magnetic permeability of the free space, ϵ_0 is the electric permittivity of free space, and $\frac{d\phi_E}{dt}$ is the rate of change of the electric flux. If the frequency is sufficiently low, the displacement current component in (2.1.1) is irrelevant, resulting in the Ampere law

$$\oint_S \overrightarrow{H}\, d\vec{l} = \mu_0 I_L. \quad (2.1.2)$$

Assuming M as a surface defined on the electric conductive material in Figure 2.1.1 and dA as the respective area, the magnetic flux translates to

$$\phi_{\overrightarrow{B}} = \int \overrightarrow{B}\, dA. \quad (2.1.3)$$

Using Faraday's law of induction with $(2.1.3)$, results in

$$\oint_M \vec{E}\, d\vec{l} = -\frac{d\phi_{\overrightarrow{B}}}{dt}, \quad (2.1.4)$$

the induced electromotive force, which generates the eddy currents illustrated in Figure 2.1.1.

2.1.2 Frequency effect

The magnetic field frequency generated due to stimulation affects how deep in the material eddy currents may penetrate. The eddy current density does not remain constant throughout the whole material. The currents concentrate at the surface, and as they penetrate the material (move away from the stimulation coil), their amplitude (strength) decreases. The decrease is exponential and is a phenomenon generally described as the skin effect [8]. The eddy currents density along depth z is

$$J(z) = J_0 e^{-z\sqrt{\pi f \mu \sigma}}, \quad (2.1.5)$$

where J_0 is the maximum surface current density, f is the stimulation frequency, μ is the magnetic permeability ($\mu = \mu_r \mu_0$), and σ is the part of electrical conductivity [11].

The frequency must be chosen according to the cracks in the material under test to allow suitable eddy current penetration. The penetration depth is higher when the frequency, conductivity, or permeability decreases. The standard penetration depth is the point where eddy currents density decreases by $1/e$ (~37%) [12] of its maximum value at the surface and is given by

$$\delta = \frac{1}{\sqrt{\pi f \mu \sigma}}. \quad (2.1.6)$$

The standard depth (δ) is often fine-tuned according to the defects under test to maximize the response signal. The thickness of the material must be two-three times the standard penetration depth, [8] since it is a rule of thumb to reduce the thickness variations interference with defects detection. When evaluating ferromagnetic materials, a high frequency is helpful to compensate for the high permeability. However, in the case of having small cracks, a high frequency is more suitable to increase the concentration of the ECs at the surface [8].

Figure 2.1.2 illustrates the ECs penetration of two magnetic fields inside aluminum for two frequencies (δ_1 = 200 Hz and δ_2=10 kHz). The effect of changing the frequency of the magnetic field is evident. A higher penetration is indeed observed for lower frequencies, as expected according to $(2.1.6)$. Regarding higher frequencies, the eddy currents concentrate closer to the surface.

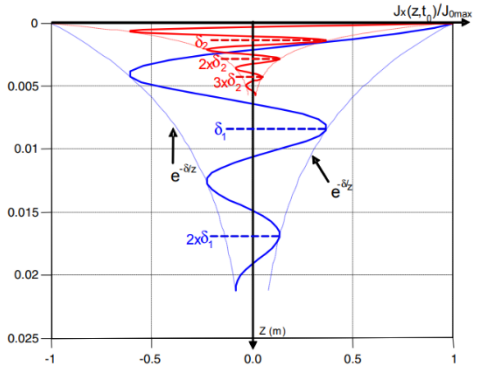

Figure 2.1.2: Penetration effect inside aluminum in [12]

2.1.3 Probe topologies

Various ECT probe topologies are employed in industry and scientific research. The distinct probes come from the different application requirements found in NDT testing. There are two categories, the separate-function probes, and the dual-function probes. The dual-function probes use the same coil as the stimulation and sensing element, while the separate-function probe has an individual coil for each task. Figure 2.1.3 presents four most common probe topologies.

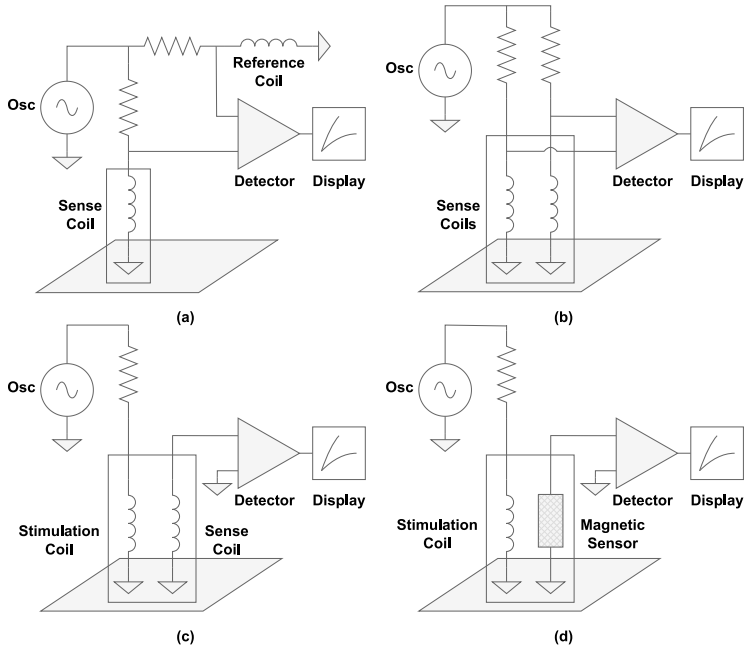

Figure 2.1.3: Probe topologies; (a) absolute, (b) differential, (c) reflection, (d) hybrid

The probes generally have a high sensitivity when the eddy currents generated are affected by discontinuities, the defects. The probes operation, according to [8], is:

- Absolute probe: uses a single coil to generate the magnetic field and measure the changes in the eddy currents. It usually has a reference coil, far from the material, to eliminate the baseline originated by the excitation primary field. This reference coil enables a high dynamic range since the voltage is null when there is no defect. Moreover, it attenuates the relation with the temperature. Besides the defects, it is possible to evaluate the materials' electrical conductivity, magnetic permeability, grain size, hardness, and stress measurement.

- Differential probe: uses two equal coils, which are responsible for stimulation and sense at the same time. These inspect close parts of the material. The coils are wound in opposite directions to remove the strong baseline. This mode of operation typically detects small discontinuities but does not detect gradual dimensional or composition variations due to the proximity between the elements.
- Reflection probe: uses two coils, one for stimulation and the other for sensing. The dedicated stimulation coil can maximize the magnetic field generated using the correct design. The same is valid for the sense, which might present higher sensitivity to the secondary magnetic field. Essentially this mode presents the advantage of optimizing each individual coil design for the purposed target.
- Hybrid probe: uses a coil and a magnetic sensor element. The coil is responsible for creating the magnetic field in the same way as the previous modes of operation. The sensitive magnetic elements might be magnetoresistive or hall sensors which can detect the secondary field from the induced eddy currents.

The topologies above illustrate the standalone fashion, which many use cases utilize. Nonetheless, using multiple coils side by side is becoming more common, creating the typically called array probes. These allow high-speed inspection of an entire 2D specimen while ensuring a good space resolution [8]. The spatial resolution depends on the sense element pitch and, of course, their size. The concept resides in using one of the topologies above, replicated, or multiplexing schemes [11].

2.1.4 Data interpretation

The interaction between a coil probe and the material under test is essential to obtain information regarding the specimen. The coil impedance variations reflect the changes in the eddy currents. The induced currents are sensitive to conductivity, magnetic permeability, and the distance between the coil and the material under test (the lift-off [8]). The presence of defects will obstruct the eddy current flow as well. As a result, the impedance plane is useful when interpreting data regarding material inspection. Figure 2.1.4 illustrates the impedance plane variations in non-ferromagnetic and ferromagnetic materials relative to the impedance in the air.

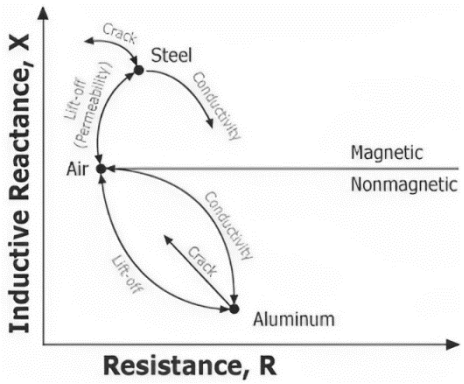

Figure 2.1.4: Impedance plane for ferromagnetic and non-ferromagnetic, adapted from [13].

The impedance plane is useful to understand and display EC data. The inductive reactance (imaginary) and the resistance (real) change depending on the material [8], [13].

When moving the coil from the air towards a non-ferromagnetic material, the resistance increases, and the inductive reactance decreases. The real part change occurs since the eddy currents will dissipate some coil power into the material. The imaginary part variation results from a weaker core coil field due to the secondary magnetic field opposition. The secondary magnetic field is reduced in a crack presence since the eddy current paths increase, and the inductive reactance and resistance revert.

The impedance changes differently when a coil gets closer to a ferromagnetic material. The resistance will also increase due to the conductive similarities. Regarding inductive reactance, the behavior is the opposite. The increase happens since the higher magnetic permeability concentrates the coil's field. The primary field overshadows the eddy currents' magnetic field. In case of a crack or conductive changes, the behavior is equal to the non-ferromagnetic material.

Typical ECT probes inspect a material under test by measuring the coil impedance variation. Besides the analog front-end used to measure the impedance, the output typically resides in a standard impedance plot [14]. This standard format provides users with an intuitive and easy way to interpret information. In the past years, more and more advanced imaging techniques have appeared. The equipment might allow the display of 2D and 3D scans, which are helpful in several applications. Figure 2.1.5 shows an example of an eddy current array used to scan an aluminum piece to detect and characterize corrosion defects.

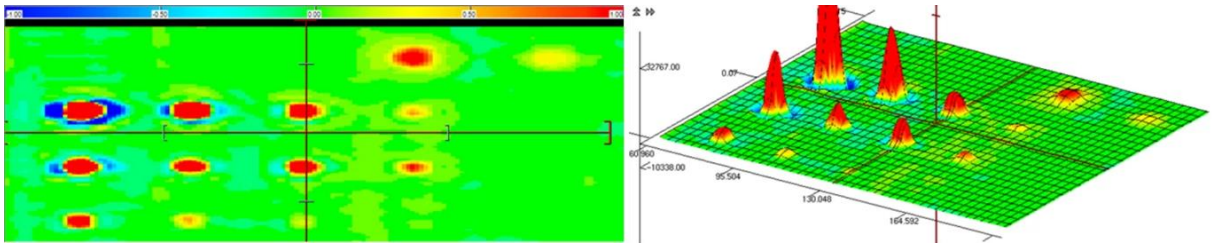

Figure 2.1.5: 2D and 3D scan of an aluminum piece in [15].

2.1.5 Instrumentation

Although compliance with the standards in the development of eddy currents equipment is typically not mandatory, it holds significant recognition across various industries. These standards serve as a mark of assurance for both suppliers and customers, indicating that specific measures have been adhered to in the development and production processes. This compliance ensures that the probes meet rigorous criteria, making them more reliable.

In the eddy currents field, several entities have established standards. Among them are the British Standards (BS) and the American Society for Testing and Materials (ASTM), which provide guidelines for magnetic flux leakage and eddy current testing methods [16], [17]. Additionally, the International Organization for Standardization (ISO) addresses several related topics as well [16], [17].

This section, however, focus only on describing the instrumentation of general-purpose eddy current equipment using the ISO 15548 perspective [18]–[20]. The standard has much more information, providing details about the instrument, probe, and system regarding the characteristics and verification. Figure 2.1.6 illustrates the functional block diagram of an eddy current instrument.

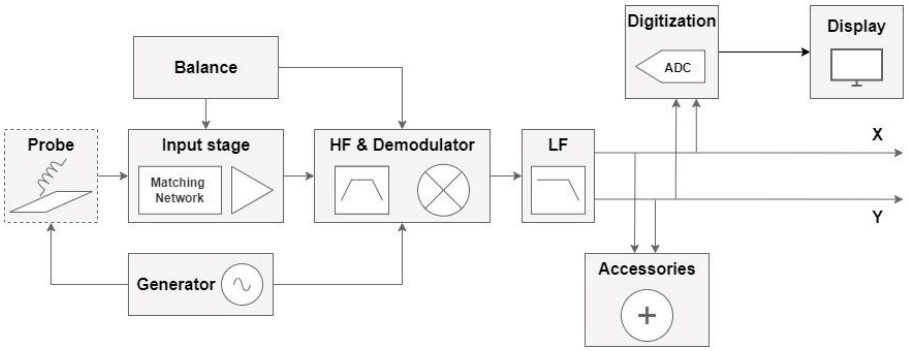

Figure 2.1.6: Functional block diagram of an eddy current instrument.

An eddy current equipment typically performs at least three essential functions: generating, measuring, and displaying. Depending on the requirements demand, the complexity might increase, and others features appear.

The primary element of the equipment is the probe. Its structure and construction are specific to the application requirements. It might use one of the probe topologies presented in previous sections. The generator is the stimulation source and can be an alternating or multifrequency source. This block is responsible for feeding the stimulation coil (driver coil) to enable the creation of the magnetic field and the eddy currents induced in the material under test.

The input stage interfaces the probe to the equipment, providing impedance matching and amplification. It refers to the first signal conditioning stage applied to the sense coil signal. The balance block is crucial in the equipment, and it consists of the equipment's compensations to set the signal in a predefined operating point. One is to remove the strong baseline expected with a reference coil, and the other is during the initial equipment calibration, the offset removal after the demodulation stage.

The High Frequency (HF) signal processing is a three-stage operation. The first is HF filtering to remove unwanted signal frequencies. It is typically a Band-Pass Filter (BPF) to suppress the signals which do not correspond to the stimulation frequency. The second is the demodulation to extract the vector components from the signal, namely the real and imaginary components. An amplification stage might appear if required. This stage extracts the low-frequency amplitude variations.

The demodulated signal goes through a Low-Frequency (LF) signal processing stage. It starts by amplifying the two signal components. Then it passes through the LF filter, typically a Low-Pass Filter (LPF) with a bandwidth dependent on the application requirements. A phase setting might conclude the stage, which allows the rotation of the demodulated signal vector on the complex plane.

The output stage characterizes the user interface. It can be a simple indicator or a screen display. The information provided might include the complex plane, time-synchronous, and imaging. The final block is digitization, and the use is optional since some devices might be completely analog. This block concerns the digital integration interface, essentially the Analog to Digital Conversion (ADC).

The generic instrumentation above remains valid in scenarios involving multiple probes or using an array composed of several sensing coils. However, the approaches typically use a multiplexed method to reduce digital demand. This technique reduces the sampling frequency, meaning the achievable resolution is lower without slowing down the recoater movement.

2.2 Powder Bed Fusion Additive Manufacturing

Metal AM covers multiple methods of building three-dimensional pieces. It is a core process in many industries nowadays, and contrary to the traditional methods, AM consists in adding material. It enables high flexibility in the design of the pieces, optimizing the geometries and reducing weight and costs. Figure 2.2.1 illustrates a great example of AM evolution, a lightweight and highly stable antenna bracket for RUAG's Sentinel Satellite made from Aluminum on the EOS M 400 system [21].

Figure 2.2.1: AM antenna bracket for RUAG's Sentinel Satellite, adapted from [21].

This work development focus on PBF printing process, which might be the most used metal AM technology worldwide. The procedure involves fusing powder particles, layer by layer, to form a solid piece. PBF uses an electron beam or more commonly laser heat sources to melt and fuse the material and form the required piece. Figure 2.2.2 shows the diagram of a typical PBF machine.

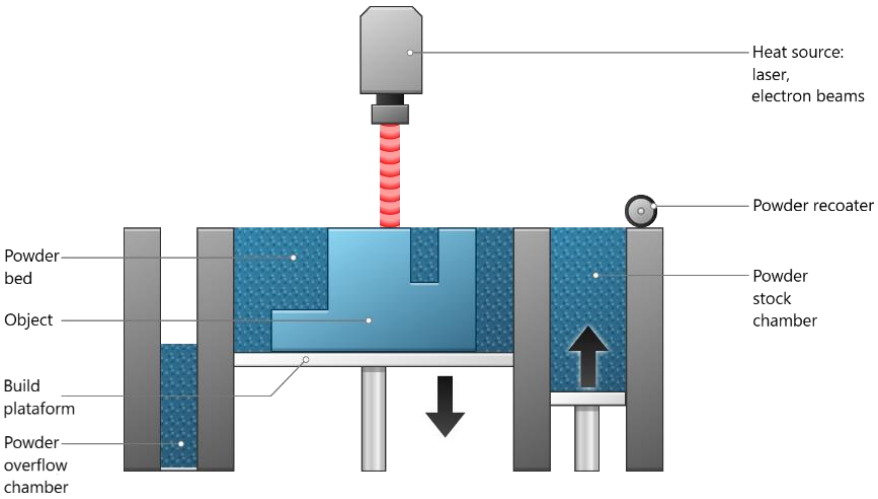

Figure 2.2.2: Diagram of a typical PBF machine, adapted from [22].

Printing a 3D piece using a PBF machine starts by filling the powder chamber with the required powder material. The chamber might be heated to reduce the energy necessary from the heat source. The re-coater then deposits (spreads) a thin layer of powder from the powder stock chamber over the powder bed (build platform). The resulting excess falls into the powder overflow chamber.

The energy source afterward melts the first cross-section of the part. After the material is solid, the elevator drops the powder chamber, and the stock chamber elevator raises. The machine in then ready for the next layer, and the procedure repeats until the part is complete.

In the realm of Additive Manufacturing (AM), a wide array of processes and methods exists, each relying on distinct physical characteristics and principles. A comprehensive overview of these diverse methods is detailed in Figure 2.2.3, offering a comprehensive overview of the existent technologies.

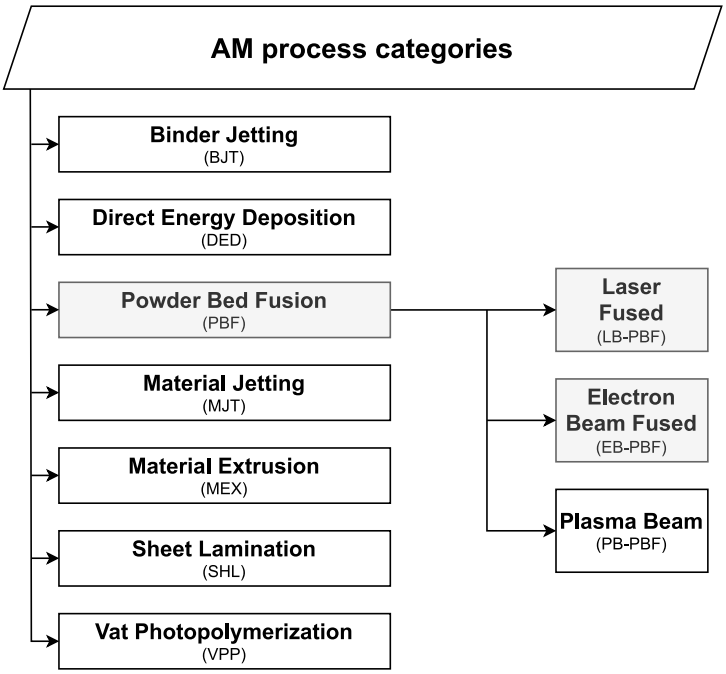

Figure 2.2.3: AM methods defined DIN EN ISO/ASTM 52900:2018-06, adapted from [23].

This work, however, focuses specifically on PBF techniques within the AM domain due to their capability to consolidate each metal layer, allowing a meticulous layer-by-layer ECT scan approach. The Laser Beam PBF (LB-PBF) and Electron Beam PBF (EB-PBF) are the methods of election for the probe developed to monitor since they are widely adopted in the industry. As elucidated by references [22] and [24], the basic concepts of the appropriate methods are the following:

- LB-PBF: the different methods in this category use lasers as the heat source to fuse the powder material. The Selective Laser Melting (SLM) reaches complete melting when heating powder. It requires an inert atmosphere (argon gas) to prevent powder from oxidizing. It might use materials like Aluminium, which creates light, robust, and unique metal pieces.
- EB-PBF: the Electron Beam Melting method uses high-energy electron beams to reach fusion. It is restricted to materials like titanium alloys and cobalt chrome but can produce less residual stress and lower distortion. Furthermore, it allows a higher speed while spending less energy: aerospace, motorsports, and medical industries commonly use this method.

The PBF process allows a low-cost production process capable of printing metal pieces with complex designs. It is an excellent asset for producing prototypes rapidly and efficiently. The major disadvantage is the lack of quality the final specimen might present since it relies on the quality and grain size of the power and the production process. These dependencies lead to defects such as gas and elongated pores with sizes ranging from 5 to 500 µm, as well as issues like balling, unfused powder, and cracking [23]. Layer-wise scanning becomes essential to study the origin and with a more complex system to control and attenuate in real time to prevent such results.

2.3 State of the Art

AM underwent a considerable change since its development for prototypes in the ’80s [25]. The disruptive technology consists of successively printing layers on top of each other in an additive fashion, contrary to the conventional subtractive methods. The process advantages are incredible in the fabrication of complex geometry with high precision, maximum material savings, flexibility in design, and personal customization [26]. Nowadays is possible to use a wide range of materials including metals, polymers, ceramics, and concrete [26].

Metal AM goes beyond the research field, industries like aerospace (e.g., turbine blades [27]), automotive, and biomedical (e.g., metal implants [28]) depend on this technology. The requirement to produce complex and functional metallic components is too demanding for traditional methods. PBF techniques are highly adopted in the printing of metals since they offer design and processing flexibility to produce end-use metallic components in a cost-effective manner [25]. The typical processes include LB-PBF or EB-PBF, which use a laser or electron beam heat source to melt specific regions of a powder layer spread with a recoater [27]. Once melting the layer, the bed adjusts, and the process repeats.

Despite all the evolution in PBF in recent years, the technology still demands more process robustness, repeatability, and stability. It is essential to use QC [29] to surpass these barriers and ensure quality to meet the requirements and certification in the leading industry sectors [30]. The QC involves evaluating and controlling the raw materials (e.g., purity, particle size), consumables (e.g., powder material, gas atmosphere), process parameters (e.g., scanning speed, layer thickness), and a sequence of predefined operations [29]. In [31], process parameters such as vector size and gas atmosphere determine the density of the metal specimen produced. Several process parameters impact, resulting in unexpected defects such as pores, high surface roughness, thermal cracking, and delamination, among others [29]. Figure 2.3.1 (a) illustrates a clear example of two internal pores of spherical shape, and Figure 2.3.1 (b) a particular case of delamination that might occur. These are only a few examples of what QC will help improve.

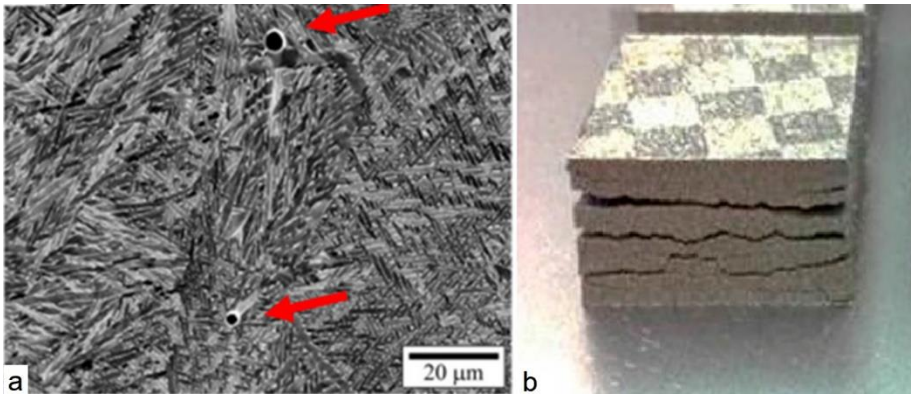

Figure 2.3.1: Example of two internal pores (a) and delamination/cracking (b), adapted from [30].

In situ monitoring is essential to perform QC layer-by-layer for detecting and avoiding defects [30], which ensures monitoring of relevant process signatures in PBF. According to the level of detail required by the process, the signatures are the melt pool, the track along the scan path, the slice (layer), and the powder bed [30]. This method allows for adjustment of the process parameters in the fabrication of the

metal piece. The ideal scenario consists of on-line process monitoring since it allows one to react immediately if the quality control does not reach the standard using feedback control [32].

Research and commercial fields have lately made on-line processes a popular theme. Nevertheless, it still requires attention since the results are still far from the industry requirements [30]. A co-axial approach in [32] implements an optical sensor set-up allowing a high-quality measurement of the melt pool. The study demonstrates the ability to monitor the process signatures by mapping each layer using a photodiode and near-infrared thermal CMOS camera to acquire. It successfully linked the pores in the produced parts to the melt pool variations. [33] reveals a similar process, In-line Coherent Imaging (ICI), to measure the surface morphology in situ. It consists in scanning an imaging beam across the metal part, collecting the backscatter, and inferring it with a reference beam. The approach enabled to QC of powder and solid layer quality, acquiring signatures such as raised areas that might collide with the recoater blade and extraction of the surface roughness.

In QC is possible to find off-axial methods as well. In [34], the system uses full-field infrared thermography to measure the relative surface temperature during cool-down to identify defects according to their thermal signature at the surface. The implementation uses a Long Wave Infrared (LWIR) camera to detect subsurface lack of fusion defects in situ. Also, [35] uses two cameras operating in the infrared and visible spectrum combining the advantage of high frame rate and spatial resolution. The configuration allows for internal defects, melt pool depth, and porosity monitoring. [36] reports an unusual approach which resides in projecting structured light and sensing it with two CCD stereo cameras to reconstruct the metal pieces layers with high precision, qualified below 10 μm.

Beyond optical sensing, it is possible to find other methodologies for QC, [37] employs Spatially Resolved Acoustic Spectroscopy (SRAS) to measure the surface wave velocity. The operation consists of sensing the acoustic waves generated in the material due to the incident pulsed laser. It enables measuring material properties and identifying surface and subsurface defect measurements to a depth of 24 μm. The study revealed that pores increase significantly with lower melting power (lower density). Furthermore, [38] proves another method to obtain 2D cross-sectional images using a laser to generate and detect ultrasound waves with a resolution of 0.5 mm. Among others, the research developments presented above, together with the clarified background of welding technologies [39] and the research to understand in greater detail the interaction between the laser and metal [40], are allowing to improve the confidence and reliability in the metal pieces produced with PBF technique.

Due to the indirect method characteristic, the previous in-situ methods present limitations in obtaining process signatures. ECT is a popular method when inspecting electrically conductive materials within the NDT category [8], [41]. The electrical conductivity measurements are closer to the material and directly related to the material properties, making ECT an attractive technology to perform online QC of PBF metal pieces. The operation concept consists of magnetic induction on the material and sensing the electrical currents. The interaction between the magnetic field and the material characteristics (e.g., defects, porosity) leads to changes in the material magnetic field and, consequently, in coil impedance changes [8]. The method is appropriate for superficial and sub-superficial crack detection [8], [42], achieving higher penetration with lower frequencies [41]. The defects characterization improves typically by using Multi-Frequency ECT (MF-ECT) or pulsed EC (PEC) techniques [43].

Numerous ECT probes may be found in the industry [8], but most aim to inspect metal surfaces after production (off-line fashion). Nevertheless, several developments targeting QC exist, [44] reports the possibility of optimizing the results by using different topologies and coils for stimulation and sensing. The optimization can lead to dedicated designs using probes unavailable commercially [45]. Furthermore, rotation or dynamic changes of the induced EC patterns enable better detection of several defects [46], [47], [48]. Within the scope of magnetic field sensor technologies, Magneto-Resistive (MR) sensors are notable for presenting a high sensitivity for weak magnetic fields, allowing for sub-surface flaw detection [41] and surface-breaking defects [47] as well.

The development in this research field has widely increased in the past years, and it is possible to find some experiments using NDT, including ECT techniques for in-situ monitoring [49]. The evaluation [50] reports the feasibility of ECT to measure relative part density variations due to the defects caused by the PBF process. It uses a standard commercial UPEC tester together with a ferrite rod coil operated in absolute mode. The study shows a strong correlation between relative part density and the ECT signal component, presenting a pathway for direct layer-wise QC. The research even progresses to mounting an ECT system of two sensors into commercial PBF-LB/M to monitor the production of four metal cube pieces [51]. Figure 2.3.2 presents the ECT signals acquired over the layers, allowing the detection of flaws resulting from process interruptions in all parts. The set of studies verifies the success of using an ECT system mounted on the recoater of a PBF machine without interfering with the production process. [52] reinforces the legitimacy of ECT equipment by measuring several process signatures, such as solidified layer thickness, track part height, and relative density.

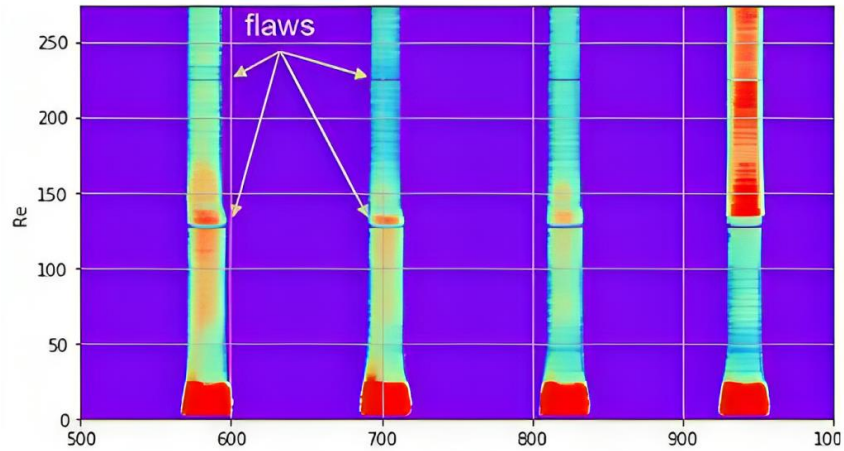

Figure 2.3.2: Vertical plane of the metal parts produced obtained by ECT, in [51].

The ECT concept of using a probe with a single sensing element is helpful in numerous cases but might present some limitations. An array probe is key for surpassing most of the constraints since they include several sensing elements allowing the capture of more information in a single pass, severely improving the detection speed and efficiency, the accuracy and reliability of the results [53]. ECT arrays enable imaging easily with a resolution dependent on the sensor's size, array spacing, and the spatial resolution of the scan [49].

One critical use case of ECT array probes consists of QC complex surfaces such as blades of steam turbines, [53] demonstrates the use of a flexible ECT array to allow defects detection in such a scenario.

The array probe uses channels made with an LC oscillator circuit to monitor the inductance changes by measuring the resonant frequency. The results provided the size, location, and shape of defects consistently compared with the actual piece through an imaging approach.

In-situ monitoring with ECT array probes is used more frequently in QC within the PBF AM industry. This method allows obtaining superficial and sub-superficial defect detection in a much effortless fashion using layer-by-layer and imaging approaches [54] while inheriting the advantages discussed above, considering the higher quantity of information in a unique readout sequence. Several years of significant development allowed the fine-tuning of the requirements for an on-line monitoring system, the main ones: being non-contact, detecting cracks and conditions; imaging for position and defect dimensions; real-time data for closed-loop control [54].

The research in ECT array probes for this application aims to increase the spatial resolution, which implies exploring different sensing elements and acquisition methods. The [54] reports a technology to detect discontinuities, surface irregularities, and undesirable process transformations in PBF-LB. The experiment uses a high-resolution commercial array probe, simultaneously stimulating all 32 integrated coils. The interleaved coils with a pitch of 0.826 mm provided proper characterization and real-time monitoring, ensuring defect detection and accurate imaging. In [55], an MR array probe uses a single-wire stimulation coil with 32 sensitive elements and a pitch of 125 μm, targeting 100 μm defects. Some developments allow optimizing the resolution and speed by using a multi-channel approach [56] or multiplexing [57]. The struggle of these implementations in [57], [58] is the inherent trade-off between resolution and readout speed with only a single readout circuitry to multiplex the 32 available sensors. Similar to [59], using an MR array with 128 giant MR elements required reducing to 1/10th (16:1 multiplexing ratio) the recoater speed to achieve the aimed 135 μm scan resolution.

This work continues the effort in [60], attempting to improve the limitations faced in the prototype development. This previous system used four microcontrollers to measure impedance from 16 coil channels independently. The concept differs from the classic approaches for achieving a simplification of the Analog Front End (AFE). It uses phase shift adjustments between the stimulation and demodulation signal to maximize the amplitude of the measured real-imaginary signal. The spatial resolution obtained was 5 mm with an acquisition rate of 20 ksps.

3. WECAP – Wireless Eddy Current Array Prototype

3.1 Overview

The Wireless Eddy Current Array Prototype (WECAP) is a demonstration kit aiming to prove the concept of layer-wise imaging over PBF specimens. The design considers the industry requirements and the existing standards mentioned in 2.1.5 to produce a powerful enough probe to scan PBF-produced parts. Figure 3.1.1 presents the elements of the probe, and Table 3.1.1 the specifications.

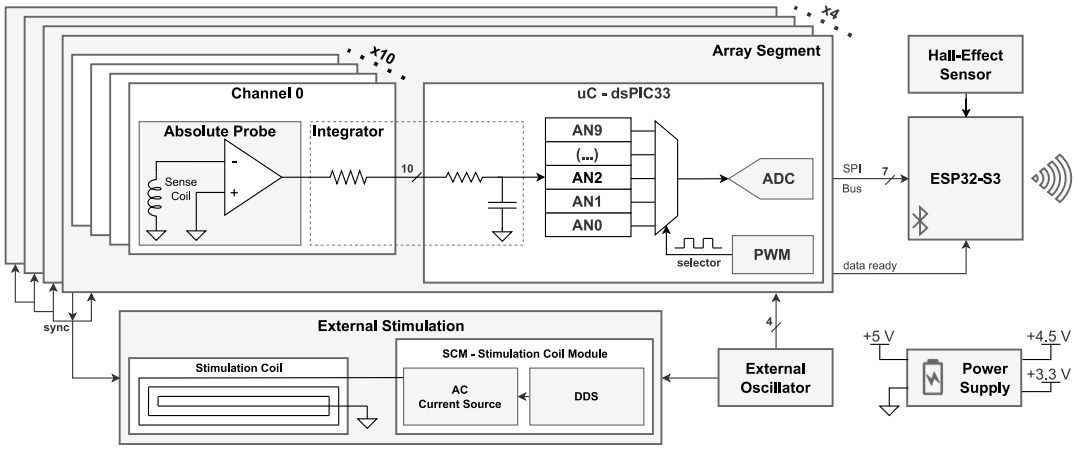

Figure 3.1.1: WECAP block diagram.

The probe architecture stands out for its minimal AFE in each channel, reducing the overall footprint and minimizing the temperature dependency while achieving a spatial resolution of 1 mm. Simplification in the probe channels circuitry appears from the stimulation and sensing electromagnetic geometry design and the external stimulation using a powerful AC current source. The probe incorporates 40 sensing coils, allowing scanning PBF layers with a length of 40 mm.

The high-frequency readout is possible using four high-speed dsPIC microcontrollers. The WECAP is an wireless device, battery-powered with data acquisition through Bluetooth Low Energy (BLE) using an ESP32-S3. The digital domain elements all share an external oscillator for synchronization. The Hall-Effect sensor is an optional feature for scan position purposes.

Table 3.1.1: WECAP overall specifications.

Dimensions	100x100 mm
Spatial Resolution (Coils pitch)	1 mm
Scan length	40 mm
Scan resolution (250 mm/s)	0.48 mm
Sampling rate	31.25 kHz
Readout Frequency	$520.8\overline{3}$ Hz
Stimulation frequency	1 MHz
Array Segment clock	180 MHz
Interface clock	240 MHz
Supply voltage	5 V
Power consumption	2.748 W

3.2 Hardware

The hardware design starts around the probe topology since it is the core element that defines the level of signal conditioning required. It aims to improve the spatial resolution to its lowest while maintaining it simple and with an overall small footprint. This section presents the hardware developed for the stimulation, readout components, and auxiliary elements.

3.2.1 Stimulation

The Stimulation Coil Module (SCM) is a PCB module developed for driving coils in general. For WECAP, its use consists in generating the array probe stimulus. A Direct Digital Synthesis (DDS) chip creates the sinusoidal signal. This signal drives the stimulation coil through a current source.

Signal Generator

The DDS element is suitable for generating a sinusoidal signal, requiring only a simple configuration. The Analog Devices AD9838 DDS, with a 28-bit phase accumulator, produces a sinusoidal signal through a 10-bit output Digital to Analog Converter (DAC). The consumption is reasonably low, achieving a maximum of 7.4 mA Figure 3.2.1 illustrates the interface with the microcontroller.

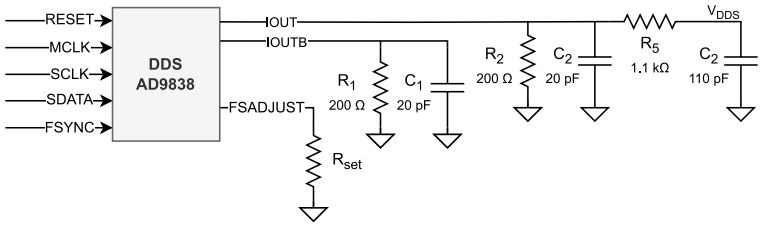

Figure 3.2.1: DDS microcontroller interface schematic.

The MCLK comes from the common external oscillator. Using the Serial Peripheral Interface (SPI) protocol, the microcontroller interfaces the DDS with the SCLK, SDATA, and FSYNC signals. The RESET pin is crucial for synchronization since it resets the internal registers to provide an analog midscale output. The present version does not consider using the other available digital pins.

The full-scale DAC current's magnitude (I_{FS}) is variable by fine-tunning the Full-Scale Adjust Control (FADJUST) resistor value, following the equation below

$$R_{set} = \frac{20{,}52}{I_{o_{FS}}}. \tag{3.2.1}$$

The chip output can operate in differential mode using IOUT and IOUTB. The design only uses the IOUT in single-ended mode. The voltage output is

$$V_{o_{FS}} = I_{o_{FS}} \times R_3. \tag{3.2.2}$$

As there is no need for deep penetration of the ECs into the specimens, given the probe layer-wise operation, the stimulation frequency in use is 1 MHz. This frequency results in a standard depth of penetration around 400 µm for stainless steel 316, allowing for scanning the surface layer and the preceding layers, considering the 60 µm thickness of each LB-PBF layer [61]. The MCLK has a frequency of 8 MHz, so the generation of the stimulation signal only uses eight cycles in the phase

accumulator. For generating a smooth signal, the high-frequency aliases produced by the DAC are attenuated using R_3 and C_3, forming an Anti-Aliasing LPF with a transfer function of

$$T(s) = \frac{\frac{1}{R_3 C_3}}{s + \frac{1}{R_3 C_3}}. \tag{3.2.3}$$

The first-order filter presents a low cutoff frequency, with a value of 1.32 MHz, which introduces some attenuation around the frequency of interest but eliminates the frequencies above the Nyquist rate.

Current source

The current source circuit takes the signal from the DDS and feeds the stimulation coil. Traditionally, a constant voltage source drives the coil, but the current flowing might not be constant due to impedance variations. The impedance might change according to the material being tested. Considering the example in Figure 3.2.2, when the WECAP starts passing over the ferromagnetic part, the electrical conductivity and magnetic permeability difference would change the stimulation coil impedance. The scan of the non-ferromagnetic part would suffer variations due to the primary magnetic field variations.

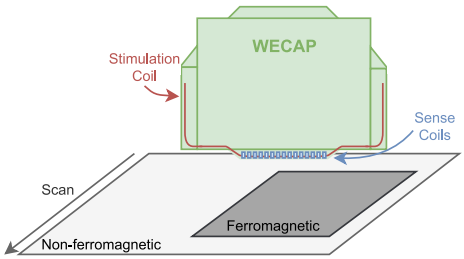

Figure 3.2.2: Scan example for stimulation coil with impedance variations.

In order to provide a constant current flowing through the coil to ensure a stationary and material-independent magnetic field, the hardware is a voltage-controlled current source with high output capability. It will provide a higher detection sensitivity since only the secondary magnetic field is expected to change with the surface inspection. Figure 3.2.3 presents the final stimulation schematic.

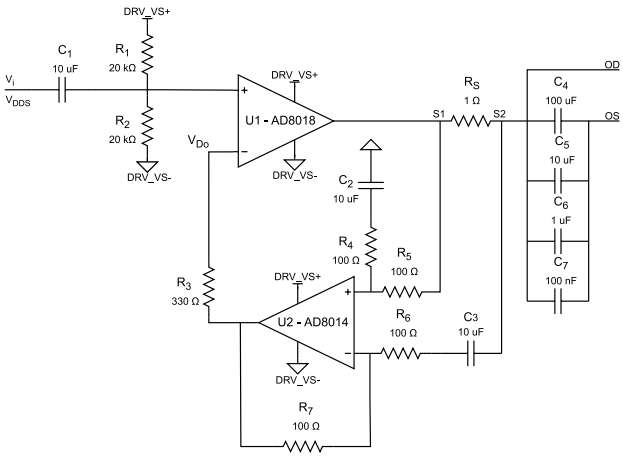

Figure 3.2.3: Stimulation driver schematic.

A current source behavior ideally provides an amplitude fixed current signal independently of the load characteristics. The design has a high-power Operational Amplifier (OPAMP) in the forward network and a subtractor topology in the feedback. A deeper analysis is beneficial to understand, starting with the subtractor equation

$$V_{D_0} = k_D(V_{S1} - V_{S2}), \tag{3.2.4}$$

with $\mathrm{k_D}$ being the subtractor gain equal to $\frac{\mathrm{R_7}}{\mathrm{R_6}} = \frac{\mathrm{R_4}}{\mathrm{R_5}}$. The equation can be simplified as

$$V_{D_0} = k_D R_S I_o, \tag{3.2.5}$$

regarding the output current and sense resistor.

Considering the virtual short and the feedback network sensing the voltage drop on R_S, the OPAMP output voltage will equal the input voltage, $V_{D_0} = V_{DDS}$. This results in the output load current being

$$I_o = \frac{V_{DDS}}{k_D R_S}, \tag{3.2.6}$$

controlled and proportional to the input voltage. If the load assumes a different value, the voltage sensed changes making the OPAMP adjust the output voltage, and the load's current is maintained within limits.

Since the current source is voltage controlled, R_{set} from the DDS plays a significant role in defining the current in the stimulation coil. According to the values of the resistors in use, the relation is 1V/1A, meaning that 400 mV at the DDS output leads to a 400 mA of peak current flowing through the load coil.

The input of the circuit biases the signal to mid-supply. It filters low-frequency components with the High-Pass Filter (HPF) made from C_1 and R_2 tunned for 0.8 Hz. In opposition, C_2 and C_3 ensure proper AC feedback without amplifying the DC component. The output DC blocking capacitors for driving the coil, with several values in parallel, ensure a low impedance path for the total operation frequency range.

The feedback network must meet the minimum Common Mode Rejection Ratio (CMRR). Otherwise, it will provide incoherent feedback of the sensing voltage, delivering a current to the load that deviates from the one in Equation $(3.2.6)$. The precautions are like the traditional high-side current sensing, where the good practices are valid for this design. First it is recommended, to use high-precision resistors, or the mismatch limits the maximum CMRR reachable. An instrumentation amplifier with the proper input common-mode range could also be an option. This design only makes use of high-precision resistors.

The forward network uses an AD8018 OPAMP, aiming for a high current output performing with frequencies up to 10 MHz. The OPAMP presents a rail-to-rail and 400 mA output current capability, with a maximum supply voltage of 8 V and a 130 MHz bandwidth. The feedback amplifier (U2), wired in the subtractor configuration, should be faster than the forward OPAMP (U1) to prevent instability and must have a high CMRR. The solution uses a low-power AD8014, with a bandwidth of around 430 MHz and a CMRR of around 65 dB at the stimulation frequency of 1 MHz.

The SCM performance is characterized according to the phase margin and bandwidth, Table 3.2.1. The simulations analyze the behavior for different PCB designed load coils. The coils' characteristics were measured using a Hioki 3522-50 LCR Meter to guarantee an accurate simulation. The equipment, unfortunately, has a maximum frequency of 100 kHz compared to the 1 MHz operation frequency.

Table 3.2.1: SCM performance simulation results.

Load characteristics		Simulation Results	
Resistance [Ω]	Inductance [μH]	Phase margin	-3dB Bandwidth
10	0	80º	26 [MHz]
4	1.13	22º	7 MHz
4.63	4.10	40º	3.9 MHz
5.81	14.62	70º	2.1 MHz
9	4.66	45º	3.7 MHz
13.21	12.65	68º	2.3 MHz
27.53	57.46	99º	737 kHz

Using a resistor as a load, the SCM has a very robust performance, but the scenario changes when using a coil. The phase margin for lower inductance values does not comply with the 45º rule of thumb. In contrast, it improves with high inductance coils, but the bandwidth is low, and the resistance value is too high, making these unsuitable for providing high currents.

The ideal scenario would be using the coil design with more turns and the maximum current flowing to provide a stronger magnetic field. The output voltage swing of the current source (4.5 V) severely limits the current. E.g., at 1 MHz, a 2 μH coil impedance modulus is ~13 Ω (ideally), meaning that 400 mA requires more than 7 V ($Z_L \times I + V_{CC}/2$), which is unfeasible. The strategy to overcome this is to place a resonant series output capacitor (C_S) to cancel out the reactive components seen by the current source at the stimulation frequency, as shown in Figure 3.2.4.

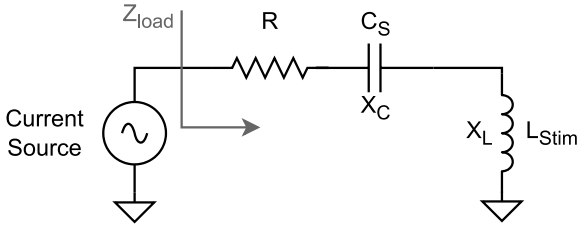

Figure 3.2.4: Series resonance circuit for enhanced stimulation.

The following equation gives the load impedance:

$$Z_{load} = R + jX_C + jX_L \tag{3.2.7}$$

At the resonant frequency $\left(f = 1/2\pi\sqrt{LC}\right)$, the reactances $X_L = \omega L$ and $X_C = -1/\omega C$ are equal and opposite, canceling each other, and the load impedance becomes purely resistive (R). The new impedance at resonance is the lowest, and the current source can deliver much higher currents since the voltage necessary to drive is low.

Considering the previous details, WECAP uses a coil design with a series resistance of 3.43 Ω and an inductance of 2.26 μH. Figure 3.2.5 displays the corresponding open-loop voltage response, showing a phase margin of 29.9 º, a value below the ideal yet stable.

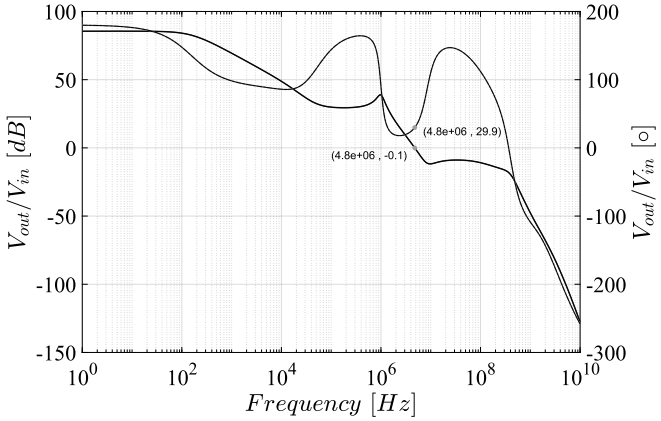

Figure 3.2.5: Stimulation driver voltage open loop frequency response.

Additionally, Figure 3.2.6 illustrates the closed-loop current response. Due to the low phase margin, it presents an overshoot, leading to a lower flat response compared to the standard -3dB bandwidth. The dashed signal represents the output characteristic of the forward OPAMP, clearly demonstrating the operation of the resonance capacitor around the stimulation frequency of 1 MHz.

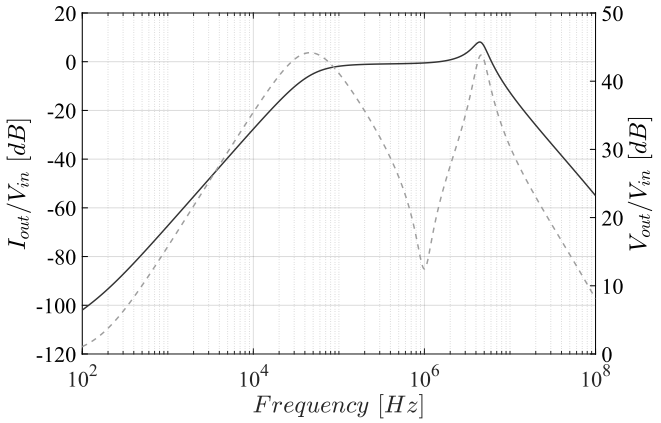

Figure 3.2.6: Stimulation driver current closed loop frequency response.

Initially, the OPAMP U2 exhibited undesired oscillations at the output. The instability resulted from the capacitance loading effect. Essentially, the inverting input of U1 introduces a capacitance that causes instability by itself. The solution added R_3, allowing to minimize the capacitance impact.

3.2.2 Probe readout

The probe readout refers to the AFE comprising the necessary hardware for adequately handling the sense coil signal. The AFE guarantees maximizing the signal according to the microcontroller characteristics. The hardware is equal for each coil (channel) to minimize the dissimilarity.

As seen in the background, usually, acquiring the signal requires several stages to get a suitable signal for inferring process parameters required by the industry. The current PCB started with a traditional design: a cancellation reference coil, a subtractor amplifier stage, a demodulator, and offset removal. However, the new approach with an external stimulation coil generating a strong magnetic field made the reading coils highly sensitive. The result of the observation led to a radical change in the AFE.

Input Amplifier

The AFE initial stage is an inverter amplifier. This stage biases the coil signal to mid-supply. The amplification enhances the signal's dynamic range to use the Full-Scale Range (FSR) of the next stage, ADC. Figure 3.2.7 presents the first stage amplifier schematic.

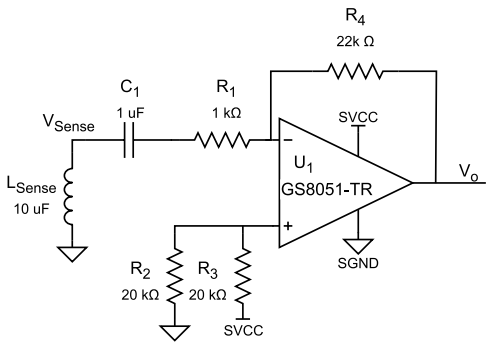

Figure 3.2.7: Sense coil inverter amplifier schematic.

The most crucial component in the stage is the sensing element. The coil is a standalone sensor used only for sensing. The primary goal is to ensure the lowest pitch possible, leading to the coil package 0402 establishing a spatial resolution of 1 mm. The coils are encapsulate-free with the maximum inductance available on the market of 10 µH, guaranteeing an appropriate acquisition sensitivity.

The amplifier topology is AC coupled, meaning only the time variant signal undergoes amplification. The C_1 guarantees only to pass the AC signal, and the voltage divider with R_2 and R_3 forces the OPAMP to replicate the mid-supply at its output. The output voltage follows the Equation below

$$V_o = \frac{R_4}{R_1} V_{Sense} + \frac{SVCC}{2}. \quad (3.2.8)$$

According to the resistors' values, the gain is 22. However, individually adjusting the gain for all 40 channels would be time-consuming. As a more efficient alternative, the approach involved precisely adjusting the stimulation current using a single resistor.

The topology has limitations in conditioning the coil signal, but it was the only topology option due to the initial PCB design. The constraints are around the input impedance of the non-inverter being substantially low, equal to R_1. Firstly, the current flowing through the sensing coil will be higher than desired, creating a magnetic field that might affect the neighbor channels. Additionally, the resulting amplified voltage is lower since using a coil with 10 µH, a frequency of 1 MHz, means 63 Ohm of impedance, not as bad as the initial 68 µH coils but still not the best performance desired.

The GS8051 has a gain bandwidth of 250 MHz, much higher than the interval of stimulation frequencies. The component also counts with a reasonable CMRR of -80 dB and an average consumption of around 2.8 mA.

Synchronous Demodulation & Sampling

The AFE final stage is the Synchronous Demodulation & Sampling (SDS) and defines the interface of the previous amplified sensing signal with the microcontroller ADC. In this phase, the signal demodulation occurs through synchronous sampling. Figure 3.2.8 represents the interface design.

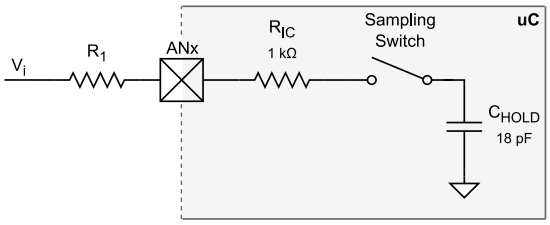

Figure 3.2.8: Stimulation signal microcontroller interface schematic.

The approach developed involves modifying the internal microcontroller ADC Sample & Hold (S&H) circuit operation concept. Using R_1 with a tuned value allows for modifying the time constant (τ) made with the capacitor C_{HOLD} to perform an integration process, as the equation below describes

$$V_{Sample} = \frac{1}{\tau}\int_0^t V_i\, dt, \tag{3.2.9}$$

with $\tau = (R_1 + R_{IC})C_{HOLD}$, valid for $t \ll \tau$. To understand the method entirely, Figure 3.2.9 illustrates a generic example. The V_{Sense} is the signal after amplification (input of the SDS), the S&H is the sampling switch activation signal, and V_{Sample} is the signal on the C_{HOLD}.

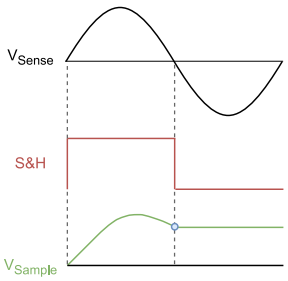

Figure 3.2.9: SDS generic example.

The example only shows a single cycle of V_{Sense}, but the process keeps occurring as long as S&H asserts to acquire measures. Usually, every time the S&H goes high, the signal on the capacitor would be a replica slightly shifted from the original signal. Nevertheless, with the design above, the result is an integration of the positive half-cycle of V_{Sense}. The concept resides in establishing a fixed point (blue dot) for sampling. E.g., When having the WECAP statically over a material, the acquired voltage is constant, but when scanning, it changes proportionally with the material conditions.

The operation resembles demodulation with a single-phase reference, with the sampling switch being the mixer. The demodulator process uses the previous array probe's model, simplifying the standard IQ demodulator. The phase rotation (time alignment) between the S&H activation and the stimulation signal allows maximizing the signal amplitude, resulting in a signal with the minimum information loss.

A complete simulation analysis initially proved the optimal value for R_1 to be 20 kΩ. At the time, the value presented the advantage of integration noise removal and having voltage values around mid-supply. However, the SDS stage was tested with greater detail, exploring the possibilities of R_1 values and S&H activation, and the conclusion was different. The optimal performance was achieved with a low integration factor, using only R_{IC} and activating the S&H to acquire sample points of V_{Sense} with 69º or 249º of phase. Essentially, the sample point aligns with either the negative or positive peak.

3.2.3 Auxiliary hardware

Apart from the core hardware described until now, the WECAP still integrates other components to guarantee its regular operation. The remaining hardware comprises the data processing, external oscillator, and power management.

Data Processing

WECAP is an embedded system designed to reconstruct PBF parts using the ECs data acquired. The probe employs four array segments to acquire signals from 40 sensing channels. These signals go through simple digital processing before being transmitted to a powerful host system.

The digital core consists of four Microchip dsPIC33CK32MC105 microcontrollers inserted in the array segments. Each acquires ten sensing signals through an internal 12-bit Successive Approximation Register (SAR) ADC, performs the digital processing required (explained later), and redirects the data through SPI. One also interfaces the DDS for initial programming. These are suitable for achieving high-speed CPU frequencies through on-chip Phase-Locked-Loop (PLL) by boosting the external oscillator source. The speed characteristic is the foremost step for solving the scanning speed constraints.

An external computer acquires the scan data using BLE. An ESP32-S3 performs the wireless operation and interfaces the microcontrollers through SPI. This interface achieves a high data output rate with a 16 MHz bit rate. A micro Secure Digital (SD) card is used as a buffer to store the scan data since the BLE data throughput is insufficient for the speed and quantity of data generated.

External Oscillator

The external oscillator is vital for the WECAP to have a proper operation. The critical point resides in sharing the clock signal among all the microcontrollers and the DDS. Using such a method allows the synchronization between the stimulation and demodulation signals. It is possible to align with zero phase shift the signals and apply phase rotation between them to improve the amplitude of the signal sampled.

Power Management

The WECAP is battery-powered with a supply voltage of 5 V and 2.748 W (549 mA) dissipation. It integrates a 5200 mAh battery, allowing continuous operation around 9 hours, enough for a demo prototype. Considering the development of an embedded system, it uses mainly 3.3 V linear regulators.

Power management in a measuring system is crucial to maintain the voltage levels within limits to ensure better accuracy in the measures. The design follows a common approach of having dedicated digital and analog voltage sources to ensure proper decoupling to attenuate the interferences. Considering the relatively low voltage supply, the regulators are LDOs with a good PSRR. The AFE regulators have a proper line regulation for lower voltage fluctuations besides having too high-power capabilities due to the intermediate design. Also, the dedicated SCM regulator is an ultra LDO since it supplies 4.5 V (very close to the maximum) for the reasons explained earlier.

3.2.4 PCB Design

The WECAP includes a PCB implementation developed under Altium Designer 16.1 and produced using JLCPCB supplier. The unique hardware concept uses a stackup of four PCBs illustrated in Figure 3.2.10 (a), forming the complete device in Figure 3.2.10 (b) with 100x100 mm dimension.

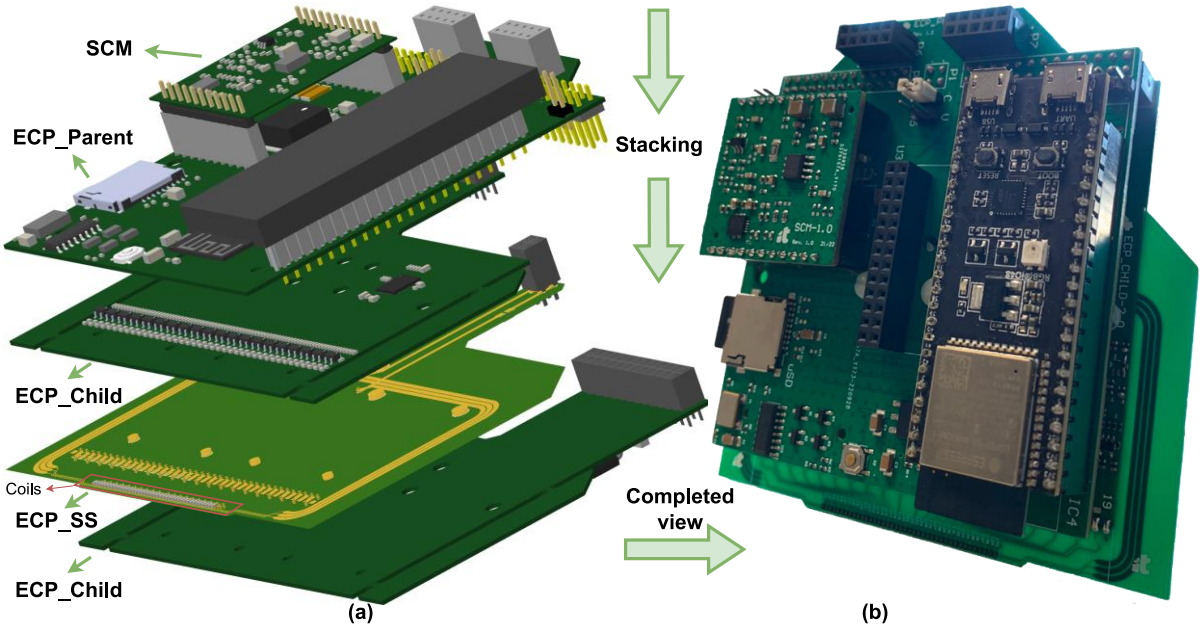

Figure 3.2.10: WECAP PCB stackup (a) and WECAP real PCB view (b).

The newest architecture splits the required hardware among several PCB designs. To understand the separation, consider the following PCB-dedicated descriptions:

- ECP_Child: readout integrating the AFE previously described and two dsPIC microcontrollers for signal acquisition. The PCB also has independent digital and analog LDOs.
- SCM: as explained earlier, is the independent module responsible for generating a voltage-controlled excitation to drive the stimulation coil with a decent performance.
- ECP_SS: the 40 sensing coils and the stimulation coil, which induces the ECs in the material under test. This PCB has two variations, the one illustrated is a three-turn design. The stimulation traces cover a wider length than the sensing line, ensuring a uniform magnetic field through all the sensing coils.
- ECP_Parent: interfaces the child PCBs, the stimulation coil, the SCM, and the ESP32-S3, providing the necessary signals. It uses a digital LDO for the shared oscillator and the microcontrollers reset circuit while having the analog dedicated for the SCM.

The initial spatial resolution target for the WECAP was 2 mm, using 0805 interleaved coils placed in each ECP_CHILD. The approach presented crucial disadvantages: first, the distance between the sensing coils and the stimulation coil, and second, their symmetrical geometry, making the scan reconstruction difficult. The new design with the smaller coils placed within the same PCB attenuates the previous problems severely while enhancing the pitch to 1 mm.

3.3 Firmware

The firmware englobes all the code development for the dsPIC microcontrollers and the ESP32-S3. The implementation goal is to keep the operations simple, ensuring that most of the processing relies on the peripherals while having the CPU with the minimum possible tasks. This way, the implementation aims for the best performance of the probe to obtain higher readout frequency without affecting the accuracy of the results. This section describes the essential considerations of firmware development.

3.3.1 Synchronization

The WECAP, as explained before, must guarantee a zero-phase shift between the stimulation and sampling signal. It is crucial to devise an accurate method for synchronization for this effect. Figure 3.3.1 presents a generic diagram of the hardware connections.

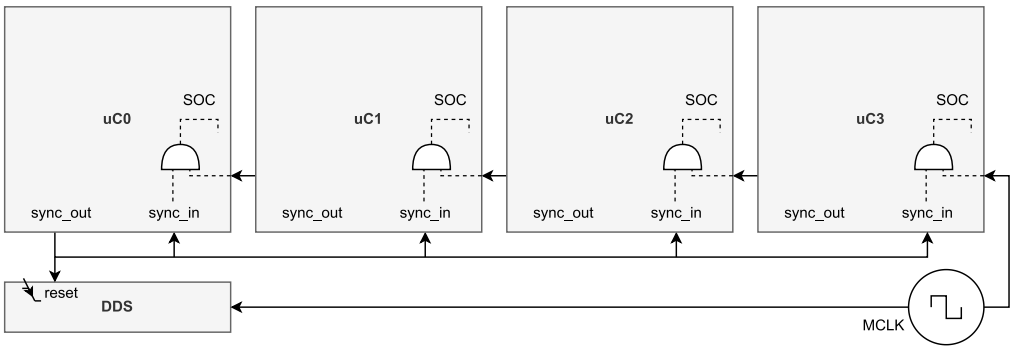

Figure 3.3.1: Synchronization hardware generic representation.

The approach shares a synchronization signal among all the microcontrollers and the DDS. The microcontroller one (master), is responsible for generating the signal at power-up. The DDS has a reset input which sets the output to mid-supply, and after the value becomes zero (sampled on MCLK falling edge), the signal restarts after an eight-clock delay. On the microcontroller side, the sync_in on the rising edge essentially triggers the start of cycle, a counter reset.

3.3.2 Stimulation

Generating the stimulation signal is less demanding for the microcontroller since it resides in the external DDS operation. The only aspect required by the firmware is the configuration.

Considering the SPI communication interface of the DDS, the implementation starts with a generic SPI driver. It is simple, with an initialization allowing to configure SPI characteristics dependent on the target and a direct write function. On top sits the actual driver of the DDS, where it sends the initial configurations, the frequency, and the phase shift of the DDS.

The stimulation frequency is 1 MHz, while the phase shift requires proper fine-tuning to ensure the sampling integration on the positive half of the sine wave. The programmed phase shift must consider the following:

- The zero-phase synchronization method delay.
- The probe input inverters in the AFE introduce 180º.

3.3.3 Probe readout

The readout concerns all the microcontroller operations required for acquiring the sensing coil signals. The architecture developed enhances the readout frequency by handling most of the operations through hardware peripherals. Figure 3.3.2 illustrates the readout stages.

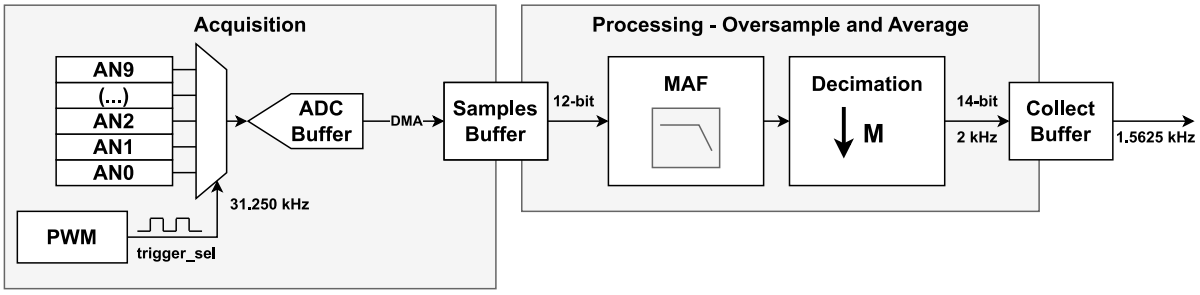

Figure 3.3.2: Microcontroller readout stages.

The readout operation has two main stages, acquisition, and processing. The acquisition block samples the analog signals using the internal ADC continuously triggered by a Pulse Width Modulation (PWM) signal. The processing consists of simple data filtering using a Moving Average Filter (MAF). The procedure of a single readout resumes on three operations:

- ADC samples and stores the ten analog channels.
- Direct Memory Access (DMA) triggers and transfers the data to a Samples Buffer.
- The CPU does the arithmetic operations of the MAF and places it in a Collect buffer.

For the high-frequency readout goal, having the microcontroller free to perform tasks like the SPI interface is crucial. The implementation only requires CPU intervention over the processing part (step 3). Below is a discussion regarding the important aspects considered while developing the peripherals.

PWM

The PWM controls the S&H of the ADC, where its frequency will correspond to the acquisition sampling rate. Additionally, it has the option to phase shift to guarantee the phase rotation according to the stimulation signal for maximizing the amplitude sampled. This characteristic is the reason for choosing the PWM peripheral because it allows operating with a frequency equal to

$$T_{PWMCORE} = \frac{\text{FPLLO}}{n}, \tag{3.3.1}$$

being the FPLLO, the PLL clock with a value of 360 MHz. It is a very high-frequency clock, allowing it to shift 180 degrees with a resolution of

$$Phase\ resolution = 360\,\frac{F_{stim}}{\text{FPLLO}}, \tag{3.3.2}$$

with F_{stim} corresponding to the desired stimulation frequency. Considering the value in use of 1 MHz, the phase resolution is about 1º. Such resolution allows the modification of the phase very accurately for better results. The driver is still missing the auto-phase calculation algorithm for initial calibration.

ADC

The internal high-speed ADC is a 12-BIT SAR with 16 analog channels. The implementation only uses ten inputs due to hardware pins and firmware limitations. The total acquisition time per channel requires attention, so the analog signals integration sample occurs as intended. The S&H circuit sampling time, the period where the switch remains closed follows the Equation below

$$T_{Sampling} = \mathrm{SHRSAMC} \times \mathrm{T_{ADCORE}}, \tag{3.3.3}$$

and the conversion to acquire the digital correspondent word takes

$$T_{Conversion} = (Bit\ resolution + 1) \times \mathrm{T_{ADCORE}}, \tag{3.3.4}$$

with $\mathrm{SHRSAMC}$ being a defined value to fine-tune $T_{Sampling}$ and $\mathrm{T_{ADCORE}}$ being the internal ADC clock.

The sum of Equations $(3.3.3)$ and $(3.3.4)$ is the total time (T_S) used to acquire the digital sample and needs to be lower than the sampling period of the PWM signal. Additionally, after a single PWM trigger, the channel samples occur sequentially, meaning after the digital word of CH0 outputs, the ADC core restarts the process for CH1 until the last one. As a result, for each analog channel sampling (integrate) the positive half of the stimulation signal, T_S must equal the period of the signal.

It is essential to increase the ADC performance by increasing the internal clock or the sampling frequency. However, neither can assume a random high value since the frequency is required to be a multiple of the stimulation frequency. Otherwise, T_S would not be equal to the stimulation period neither the sampling trigger would equal the initial point of the input sine waveform.

DMA

The peripheral DMA resides in a simple concept but with a significant role in the microcontroller operation. After the ADC finishes acquiring the ten channels, the DMA receives a trigger and handles the transference of the digital words to a dedicated buffer through hardware. It is essential since the CPU can service peripherals that are not on the DMA bus. This way, the CPU can perform other tasks without stalling, increasing the effective bandwidth for handling data.

Processing

The processing stage employs an oversampling and averaging method to increase the output estimate resolution and Signal-to-Noise Ratio (SNR). This concept operates on the principle that oversampling the input signal increases the resolution. According to the Nyquist frequency

$$f_n = 2 \times f_m, \tag{3.3.5}$$

with f_m equal to the highest frequency of interest (bandwidth), any sampling frequencies (f_s) above f_n is considered oversampling. According to [62], the Effective Number of Bits (ENOB) increase follows

$$f_{OS} = 4^w \times f_s, \tag{3.3.6}$$

where w represents the number of additional bits, f_{os} is the oversampling frequency, and f_s is the original sampling frequency (f_n). For each additional bit of resolution, the oversampling increases the sampling frequency factor by four, defined by the Oversampling Ratio (OSR).

Considering using a f_m equal to 1 kHz to detect structures as small as 0.26 mm at a recoater speed of 250 mm/s, the sampling frequency required is 31.25 kHz, the closest suitable for the SDS operation, allowing to gain two extra bits. The next step indicated in [62] is decimation, accumulating (sum) enough samples and dividing the total by 2 (two right shifts). The decimation part uses the MAF defined below,

$$y[i] = \frac{1}{w}\sum_{j=0}^{M-1} x[i-j], \tag{3.3.7}$$

where x is the input signal, y is the filtered signal, and w is the extra bits gained. The MAF equation traditionally used the number of samples accumulated in the denominator, but to scale the signal correctly, it uses the number of additional samples [63]. Figure 3.3.3 illustrates the frequency response.

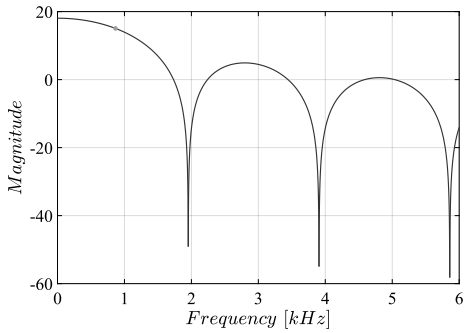

Figure 3.3.3: MAF response.

The resulting filter accumulates 16 samples, yielding a cutoff frequency at 866 Hz. Considering the oversample and average (decimate), the throughput is lowered to 2 kHz, since f_s is reduced by OSR.

3.3.4 Data interface

The data interface connects the four high-speed dsPIC microcontrollers to the ESP32-S3 through SPI. Figure 3 illustrates the design to perform such an operation.

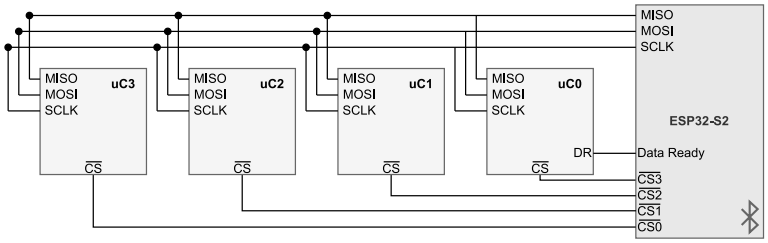

Figure 3.3.4: SPI bus configuration for ESP32-S3 data interface.

The configuration chosen is standard, commonly known as cascade mode. The communication bus is shared among all the microcontrollers and has individual Chip Select (CS) for independent access. An integral aspect of the slave firmware development is the data-ready pin. The full-duplex SPI transmission uses two DMA channels. However, since the data readout uses another channel, the operations could not overlap, or one of the operations would be affected. The approach provides a data-ready signal that triggers at the end of each acquisition, making both processes possible to co-exist. This signal has 1.5625 kHz frequency to align with the data throughput after decimation. Considering a

250 mm/s recoater speed and the readout frequency established, the scan resolution would be at 0.16 mm $(250\ mm/1.5625\ kHz)$.

However, due to the latency in the ESP32-S3 within the process of attending to the data-ready trigger, performing the SPI transfer, and asserting the necessary variables, the newer trigger could not be attended in time. This bottleneck led to performing a conservative access, as illustrated in Figure 3.3.5.

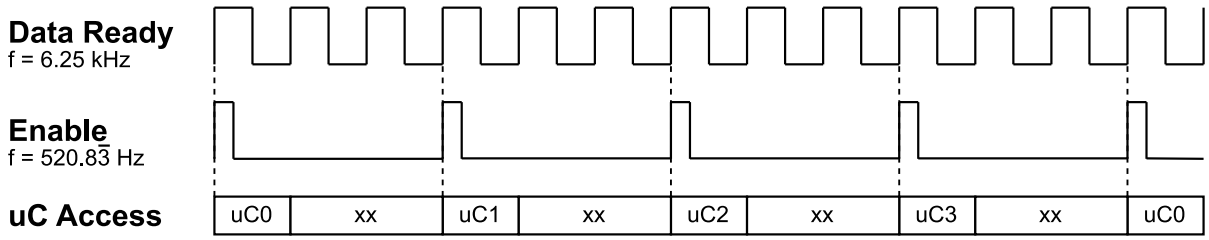

Figure 3.3.5: Generic time diagram of ESP32-S3 data transfer.

The data transfer occurs every three cycles of the data-ready signal, meaning the resolution is lower. Considering the same recoater speed target and the 520.8$\bar{3}$ Hz readout frequency, the scan resolution stands at 0.48 mm $(250\ mm/520.8\bar{3}\ Hz)$, translating to half the spatial resolution.

3.3.5 Wireless interface

The Wireless interface fully uses the ESP32-S3 capabilities to achieve such an anticipated goal. Firmware development was one of the most challenging parts of the WECAP, but it was simplified using the Espressif Software Development Kit (SDK). The architecture uses the FreeRTOS operating system kernel to manage concurrent threads integral to the system's operation.

The initial approach planned to use the Serial Port Profile (SPP) from Classic Bluetooth. This native profile would have enabled a fast integration with the LabView Software, emulating the device as a serial cable connection. However, for improved SPI performance, the ESP32-S3 was selected. This microcontroller offers only BLE capabilities, thus lacking a native option for direct emulation of SPP.

The solution begins by defining the devices' role to function as a peripheral within the network, utilizing the Generic Access Profile (GAP) capabilities. Subsequently, the device effectively simulates two distinct communication channels as serial communication: one for writing data and another for reading. This emulation is achieved by establishing two crucial characteristics within the Generic Attribute (GATT) services table, namely the Receiver (RX) and Transmitter (TX). On top of this, the solution incorporates a third-party Python library on the computer side. This library facilitates selecting specific characteristics and maps them onto the appropriate COM Port channel.

The second development phase centered on integrating the SPI master, which orchestrates the transmission of commands received from the host and the collection of scan data. Given BLEs' inherent low data throughput, a micro-SD card serves as a buffer for acquired samples. The host only receives these samples upon completion of the scan process. A dual-core configuration is employed to mitigate the significant overhead the BLE stack introduces on the microcontroller. One core is dedicated to managing the BLE stack, while the other focuses on data management.

3.4 Software

The WECAP user interface represents a sophisticated computer application developed using the LabVIEW Software capabilities, as shown in Figure 3.4.1. This new application, developed from scratch, simplifies the legacy version, providing easy integration with several inspection systems.

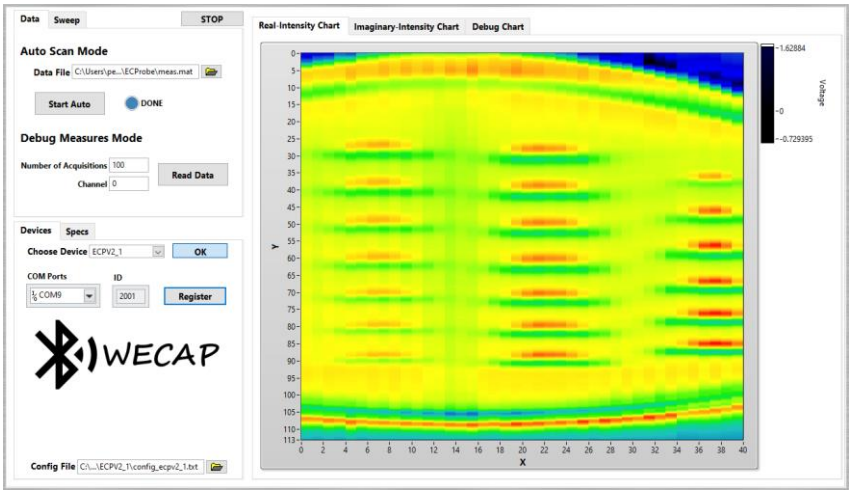

Figure 3.4.1: GUI to control the WECAP and CNC.

The implementation uses a parent probe class with pre-defined empty functions (LabView VIs) such as initialization, command transmission, data retrieval, and close. When installing a new device, the only requirement is to develop the drivers or even inherit some functions from other probes for simplification. Furthermore, some graphical tabs adjust dynamically based on the probe, facilitating the display of different connection types, configuration parameters, and calibration methods. The users only need to select the appropriate drivers during the operation.

Regarding the WECAP, starting the scan acquisition requires two steps. The first involves configuring the phase rotation parameter, while the second is calibration. Calibration requires placing the probe in the air and over metal to capture data samples, which are then used in the reconstruction process to compensate for channel mismatches and sensitivity variations.

The application also maintains the Computer Numerical Control (CNC) control capabilities since other inspection probes rely on it for achieving higher precision scans. This portion of the software has remained unchanged, except for its update into a class structure and enhancements to improve speed. It continues to support manual and automatic control of the probes' position.

3.5 Probe Demonstrator

The WECAP demonstrator aims to provide users with an effortless and intuitive process of scanning specimens produced with PBF. Figure 3.5.1 presents the demonstrator built to integrate the WECAP.

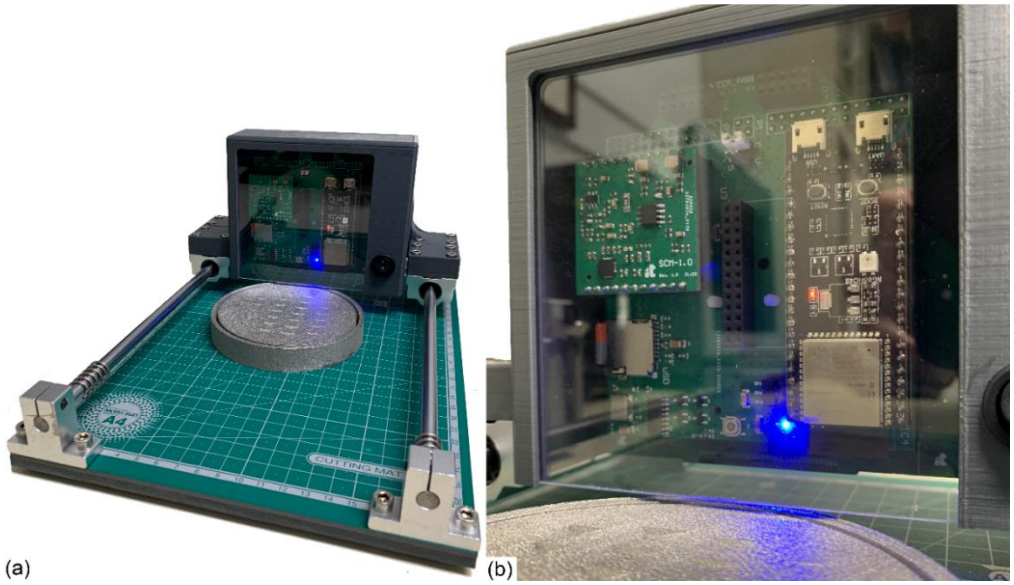

Figure 3.5.1: Probe demonstrator (a) and WECAP close-up (b).

This setup features a scan area of 173x40mm, allowing users to manually pass the WECAP over any object. It includes a non-slip base with a grid to align the objects correctly. It also uses two linear guides for smooth and vibration-free scans, with springs at the ends to dampen any impacts on the probe.

The device requires configuration and calibration before performing scans. The operation comes down to pressing the start button in the application, moving the probe, and pressing the button again. The software automatically zooms in on the specimen, ignoring the empty areas. The equipment also contains a hall-effect sensor that can detect the start and end of the scan. However, it is currently deactivated due to the magnets required in the scan area, which may obstruct the scan area.

4. StrixVision – Advanced Eddy Current Array Probe

4.1 Overview

The StrixVision is a complete ECP array aiming to enter the AM industry to QC PBF process parameters layer-by-layer. It is an upgraded and more powerful version of WECAP, improving the less optimal characteristics while enhancing the scan length and the resolution capabilities. Figure 4.1.1 and Table 4.1.1 present the new block diagram and probe specifications.

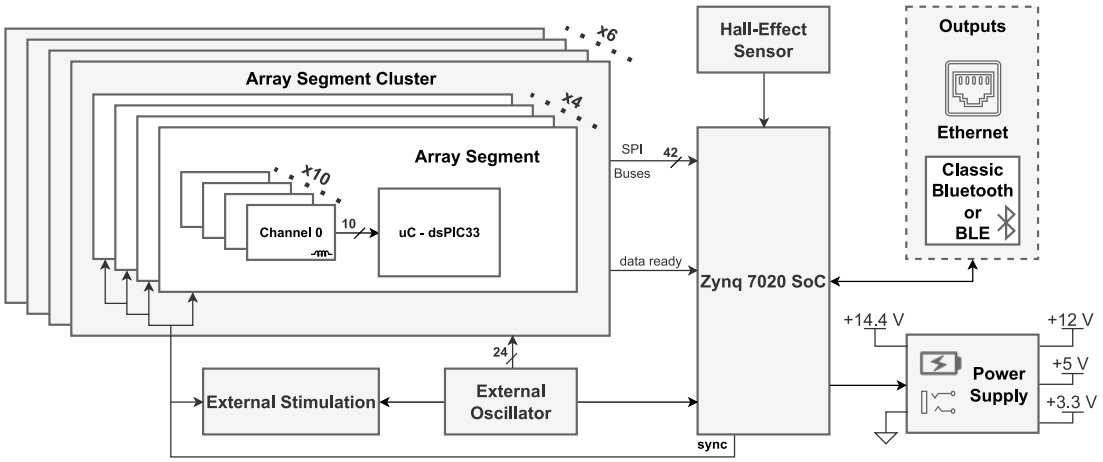

Figure 4.1.1: StrixVision block diagram.

The developed architecture grows on top of the previous version core, with the main difference residing in scaling up the number of Array Segments from 4 to 24, with several stacked side by side. The electromagnetic geometry between stimulation and sensing is very similar, with upgrades only on the PCB design. The AFE, on the other hand, suffered upgrades to solve the previous limitations.

Currently, the device design supports 240 sensing coils, requiring 24 dsPIC microcontrollers for sampling, leading to a massive data amount with considerably high throughput. To keep up with the massive processing demand, StrixVision uses an Zynq 7000 System on Chip (SoC) to retrieve the six Array Segment Cluster data in parallel. The device operates in wireless mode using a 9800 mAh battery with a data interface through Bluetooth or cable mode with mains power and ethernet output.

Table 4.1.1: StrixVision overall specifications.

Dimensions	250x97 mm
Spatial Resolution (Coils pitch)	1 mm
Scan length	240 mm
Scan resolution (250 mm/s)	0.16 mm
Sampling rate	31.25 kHz
Readout Frequency	1.5625 kHz
Stimulation frequency	1 MHz
Array Segment clock	180 MHz
Interface clock	666 MHz
Supply voltage	10 V
Power consumption	12.89 W

4.2 Hardware

The hardware design of the StrixVision is a refinement of the WECAP design. The insights gained during the previous development allowed the identification of the critical enhancements required to achieve a more robust design while keeping the primary goal of a compact device. The chapter shows the modifications made and introduces the new features incorporated into the new design.

4.2.1 Stimulation

The core component of WECAP, the dedicated SCM, remained unchanged due to its decent performance in driving independent stimulation coils, particularly with the resonant capacitor, enabling compatibility with a wide range of coils. Only two factors had the potential to affect its regular operation: the maximum rated supply voltage and the CMRR of the feedback network.

The main concern revolved around the maximum voltage limit of 5 V. The new stimulation coil configuration covers a significantly larger scanning area, resulting in a longer coil length and higher impedance. Sustaining the capacity for driving the coil with a high current to generate a strong primary magnetic field with such a low voltage could be challenging.

Regarding the CMRR, the goal was to enhance it by replacing the feedback OPAMP with an instrumentation amplifier for precise current sensing. However, before modifying the working topology, the performance was evaluated using a sinusoidal signal across a 10 kHz to 1.4 MHz frequency range. CMRR was assessed by comparing feedback voltage (expected load current) to the 1 Ohm load voltage. Results indicated minimal CMRR impact on load current, with the deviations at a maximum of 5%.

A newer SCM version with updated components has been developed, operating with a power supply rated at 12 V, delivering 1.2 A output. This design aims to drive the stimulation coil and generate a stronger magnetic field. However, due to time constraints, validating its performance was not possible.

Currently, the device uses a coil design with 0.15 mm width in the sensing area. The remaining path uses two layers with 3 mm to decrease the resistivity, resulting in a resistance of only 5 Ω. This allows driving the coil effortlessly with 700 mA, all without the need for the resonant capacitor.

4.2.2 Probe Readout

The current AFE, like its predecessor, connects the sensing coil to the microcontroller ADC channel input. This design uses an AC-coupled non-inverter amplifier topology, as illustrated in Figure 4.2.1.

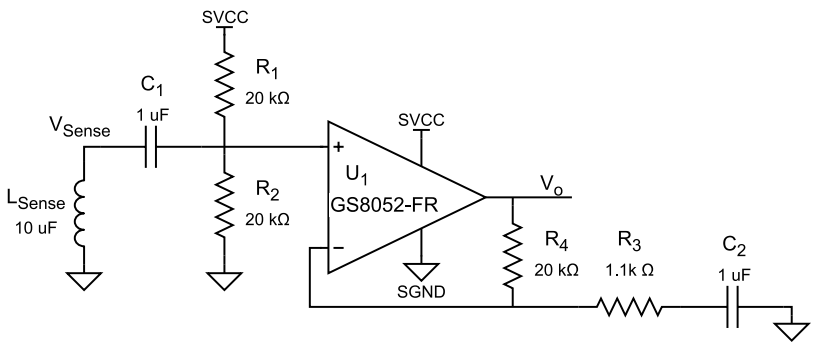

Figure 4.2.1: Sense coil non-inverter amplifier schematic.

The topology operation is simple, starting by the coupling capacitor C_1 removing any DC voltage from the input signal. Subsequently, the resistive voltage divider created by R_1 and R_2 defines the voltage input to one-half of the power supply. The feedback capacitor, C_2, prevents DC amplification, buffering it to the output through the feedback resistor. The feedback network defines the AC gain according to

$$V_o = \left(\frac{R_4}{R_3} + 1\right) V_{Sense} + \frac{SVCC}{2}. \quad (4.2.1)$$

The gain value employed is around 20, a value very much in line with its predecessor. This choice was validated as it effectively produces a signal close to the power supply rails while having a powerful primary magnetic field stimulation. Notably, C_1 and the parallel combination of R_1 and R_2 form an HPF tunned to 16 Hz, ensuring a flat frequency response around the stimulation frequency.

The rationale behind adopting this new topology arises from the limitations presented earlier. Most notably, the input impedance is ten times higher, attenuating the loading effect on the source signal to acceptable levels. Furthermore, the topology separates the feedback network from the input, facilitating the maintenance of low resistor values for reduced noise. Additionally, this configuration eliminates phase inversion, simplifying the synchronization process. It is worth noting that the OPAMP is the same, with only the package being switched to a dual OPAMP option to reduce the overall footprint.

The ideal scenario for this AFE, attending the SDS operation, would be to sample only the positive part of the sinusoidal signal to produce higher-resolution samples. However, this approach would increase circuit complexity and, consequently, the overall footprint. An alternative explored involved removing mid-supply bias from the previous topology, allowing the OPAMP to saturate during the negative portion of the signal. However, this led to undesirable consequences, including recovery delay and signal distortion, making it an unacceptable choice.

4.2.3 Auxiliary Hardware

Up to this point, the hardware discussion revolves around the acquisition and stimulation stages, the core of the sensing interface. Below are the remaining hardware elements responsible for data processing, external oscillator, and system power management.

Data Processing

The StrixVision aims to reconstruct the PBF specimens in a 3D fashion, using the scans gathered in each layer of the construction process. The data acquisition relies on the array segment cluster, a design mostly inherited, with dedicated microcontrollers acquiring data from 240 sensing channels.

The latest addition to the setup is a Zynq-7000 SoC. The importance of this addition lies in its capability to acquire data from multiple microcontrollers simultaneously through SPI. Specifically, it enables data acquisition from 24 microcontrollers, with the ability to communicate with six in parallel. This parallelism accelerates data acquisition and improves the previous scanning resolution while increasing the coil number from 40 to 240. The SoC incorporates a dual-core ARM Cortex A9 in the Processing System (PS) and an Artix-7 equivalent in the Programmable Logic (PL). The main features of XC7Z020-2CLG400I are summarized in Table 4.2.1.

Table 4.2.1: XC7Z020-2CLG400I SoC specifications.

PS	Maximum Frequency	766 MHz
	On-Chip Memory	256 KB
	External Memory Support	DDR3
	Peripherals	UART, SPI, GPIO
	Peripherals with built-in DMA	USB 2.0, Gigabit Ethernet, SD/SDIO
PL	Logic Cells	85 k
	Look-Up Tables (LUTs)	53,200
	Flip-Flops	106,400
	Block Random Access Memory (BRAM)	4.9 Mb
	Maximum I/O Pins	200

Designing a PCB to accommodate an SoC was out of the equation since it is a complex development with several challenges to guarantee an appropriate operation. Instead, the device uses a complete design board, the Z-turn Board V2. This board was carefully selected to meet StrixVision requirements, access to numerous I/O pins, onboard memory for data retrieval, and ethernet connectivity.

Ultimately, the collected data is transmitted to a host computer for scan data processing, with two options available for the two operation modes. The mode depends on the host interface capabilities and the PBF printer limitations. The Z-turn Board Ethernet port facilitates data transfer when powered by the mains. However, when operating wirelessly on battery power, the FPGA communicates via UART with CYBT-343026-01, a versatile module capable of supporting both Classic Bluetooth and BLE.

External Oscillator

The approach of utilizing an external common oscillator across all digital elements remains in this new version. However, the board now offers the flexibility to either select an 8 MHz or 16 MHz oscillator. It predominantly aims to improve the SCM signal resolution if necessary.

Power Management

The probes' power design is crucial to ensure a stable operation, especially given the substantial hardware expansion compared to its predecessor and the expected consumption of around 2.8 A.

When using a battery or mains power source, the power supply input ranges from 10 V to 15.5 V. To efficiently power the SoC and the array segment cluster, two dedicated DC-DC regulators step down the voltage to a stable 5 V level. This conversion minimizes power dissipation and extends battery life.

Each array segment maintains the LDOs' approach, decreasing the voltage from 5 V to 3.3 V. This design choice allows the attenuation of any noise and ripple the DC-DC might introduce. The SoC board already comes with dedicated regulators ensuring its operation. The SCM benefits from a dedicated LDO that steps down from 10 V to 5 V. While this approach may not be highly efficient, it produces a steady high voltage, allowing the generation of a robust current signal to drive the stimulation coil.

The probes' final power consumption is around 1.289 A using 10 V (12.89 W) when supplied from mains or a 9800 mAh battery. This comprehensive power management guarantees reliable operation.

4.2.4 PCB Design

The StrixVision PCB, designed using Altium Designer 23.6, uses an eight-PCB stackup to guarantee a small form factor, measuring only 250x97x34 mm. Figure 4.2.2 (a) and (b) exhibit the 3D models from the front and back perspectives of the device, respectively.

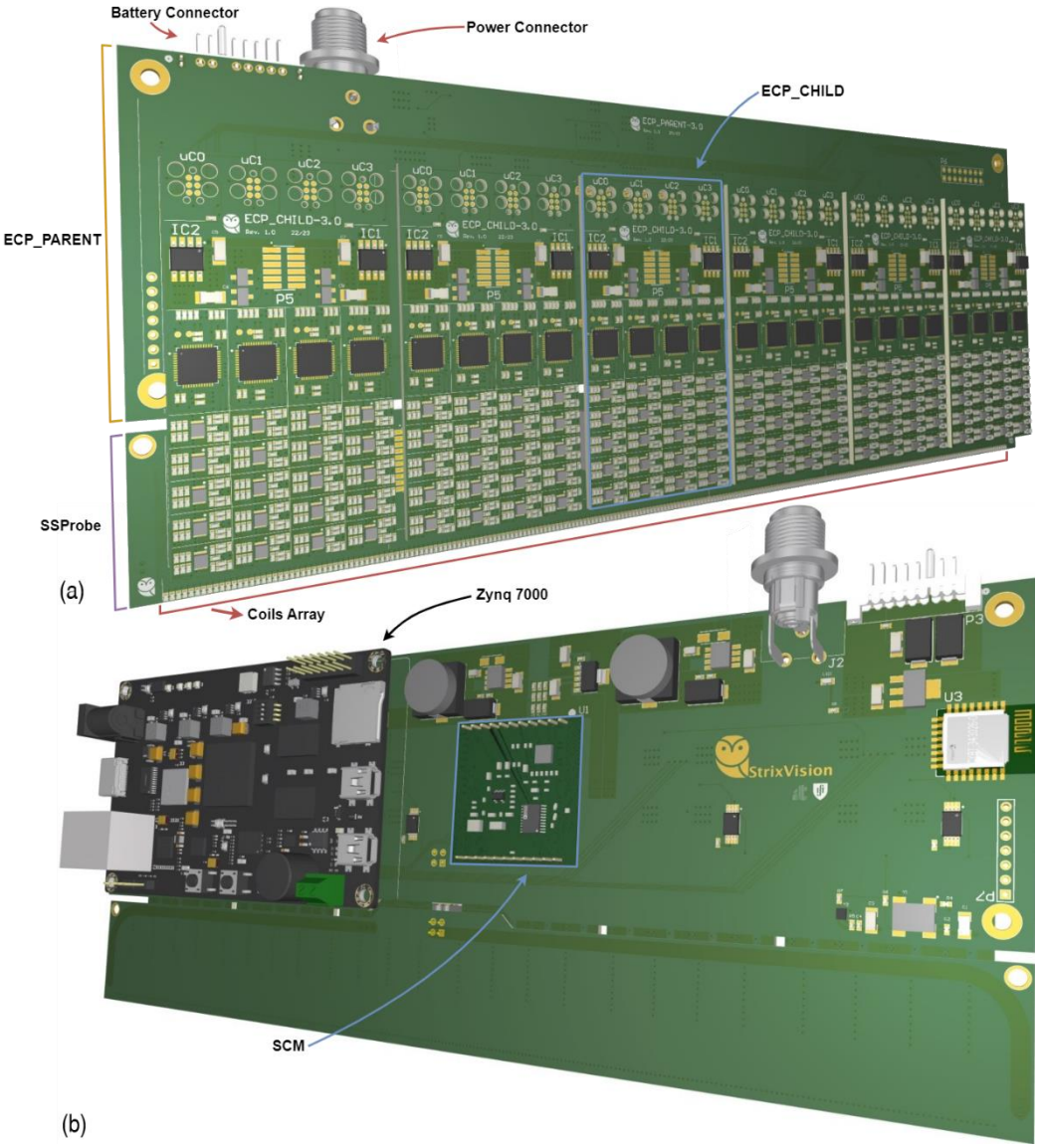

Figure 4.2.2: StrixVision PCB front view (a) and back view (b).

The hardware separation between the three distinct PCB designs follows the WECAP concept. The architecture allows the different PCBs to be replaced independently without requiring a complete redesign. Most important is the ability to switch between different stimulation and sensing electromagnetic geometries to improve the results depending on the specimens in production.

Concerning the PCBs, the SSProbe integrates the stimulation coil and the sensing coils spaced by 1 mm. The ECP_Childs, referred to as Array Segment Cluster, have all the necessary readout hardware. Meanwhile, the ECP_Parent is responsible for power management, connecting all the PCBs, and incorporating the SoC, the SCM, and the future Bluetooth module. The connections are made through low-profile connectors to reduce the overall height, resulting in a compact design.

4.3 SoC Integration

The integration of Zynq-7000 into the system results from the demand for parallel processing to handle the amount of data generated by the array segment cluster, aiming to maintain the predecessor scanning resolution. The development process for the SoC includes two main components, the hardware description for the PL using VHDL and the firmware for the PS using C language. Figure 4.3.1 illustrates the general functional blocks of the architecture designed for the StrixVision application.

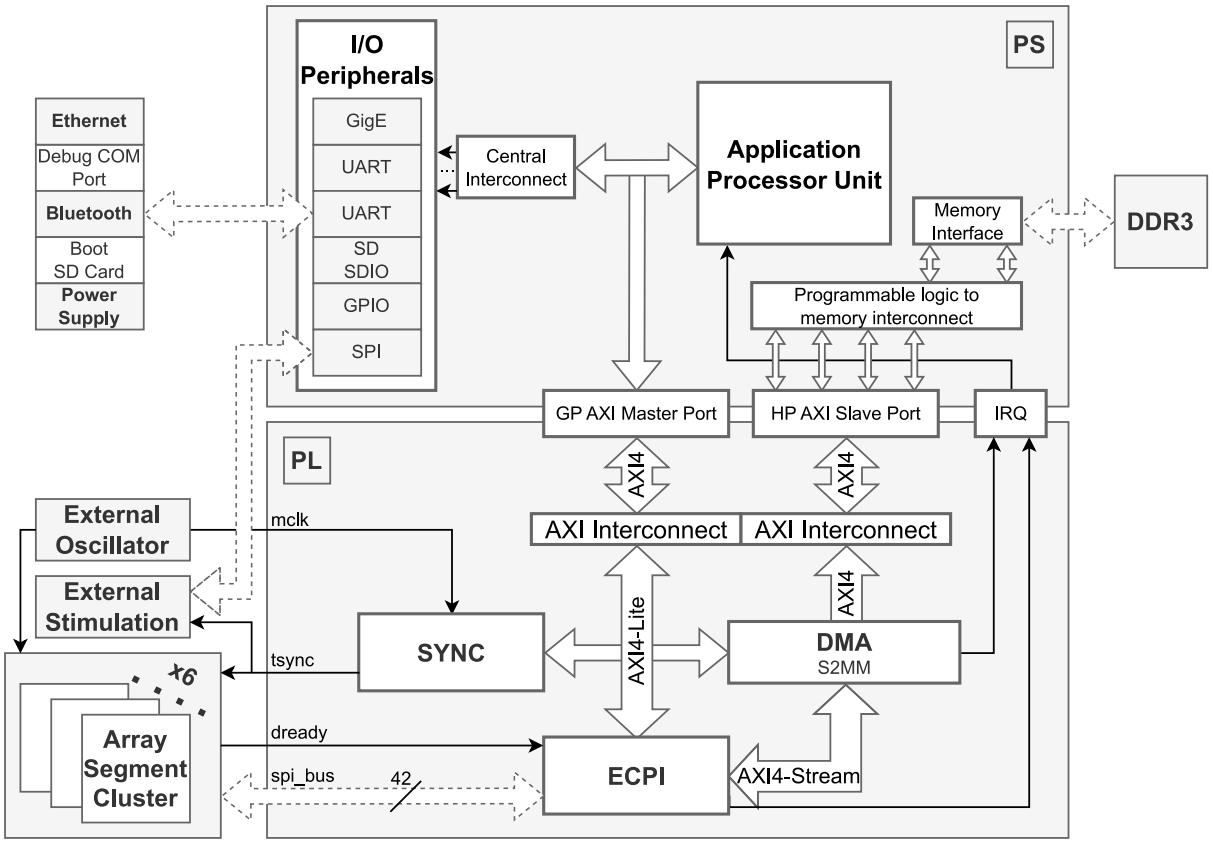

Figure 4.3.1: Zynq-7000 SoC architecture block diagram.

The Xilinx native tools, the well-known Vivado 2022.2 and Xilinx Vitis 2022.2, allowed a very efficient development process. Vivado facilitated the design of Intellectual Property (IP) cores, including modules from scratch like Synchronism (SYNC) and Eddy Current Probes Interface (ECPI) and configuring pre-existing IPs such as DMA and the ARM cores. On the other hand, Xilinx Vitis supported the implementation of the firmware component, which is responsible for managing all the IP cores in use, the necessary PS peripherals, and the ethernet stack.

The system follows a bare-metal approach using a single core. It comprises four main processes: power management, digital synchronization, data acquisition and storage, and host interface. The PS and PL sides are actively responsible for performing these processes, with the PL responsible for the most demanding tasks. Communication between the PL and PS or between IP cores occurs through the standard Advanced eXtensible Interface 4 (AMBA AXI4) defined and controlled by Arm. This section provides detailed explanations of each process implementation.

4.3.1 Power Management

The power management operations are simple features offering significant advantages. All the regulators can be enabled or disabled as required. The system starts with all regulators disabled, activating them only during the scans. This approach extends battery life and prevents unnecessary energy consumption, especially considering the layer scans occupy a significantly lower percentage of total production time. As a result, only the SoC is functioning during the idle state.

Additionally, the system follows a safe power-up sequence. Regulators are enabled sequentially to prevent a significant current peak. The control is obtained through the Extended multiplexed I/O interface (EMIO), redirected from the PL to the PS, allowing a simple pin state management through firmware.

4.3.2 Digital Synchronization

Digital synchronization is mandatory considering the SDS concept, a feature already embedded in the WECAP version. Previously, the method relied on a master microcontroller within the array segment. However, the SoC offers a more accessible and flexible solution. The concept remains the same, it uses the shared oscillator signal (*mclk*) to generate a trigger for the DDS and the dsPIC microcontrollers to guarantee synchronization between the stimulation and the demodulation with a deterministic delay. Programming the DDS also shifted to the SoC Arm core responsibility.

Most of the operation occurs on the PL side. A simple state machine generates a trigger signal (*tsync*) upon a rising edge of the shared clock with a predefined high duration. The PS is responsible for writing to an internal module register to start the synchronization and then waits for the high-status bit to indicate the operations' completion. Communication between the PL and PS takes place through the AXIS-Lite bus, a lightweight version of AXI4 allowing the read and write operations of internal SYNC registers.

4.3.3 Data acquisition and storage

Data acquisition and storage are the core processes in the system and are the primary reasons for integrating the SoC. ECPI is the IP core designed to acquire the sensing data from all the microcontrollers. Additionally, it is responsible for handling the transmission of the configuration commands received from the host. Figure 4.3.2 illustrates the ECPI functional blocks.

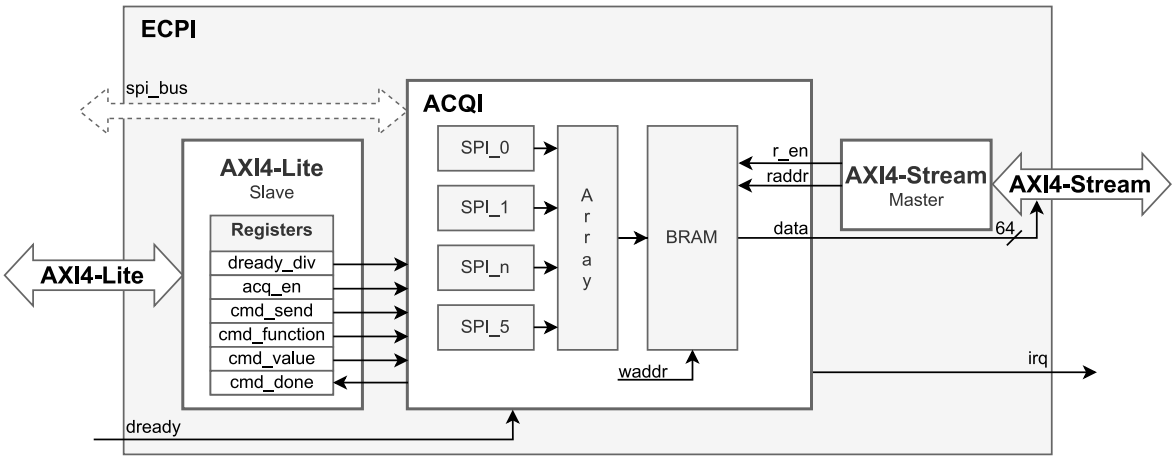

Figure 4.3.2: ECPI architecture block diagram.

The PS side configures and controls the IP behavior through the AXI4-Lite slave interface. The AXI4-Stream interface is a high-performance streaming interface that allows faster transfer of the acquired data for further storage. However, the primary operations occur under ACQuisition Interface (ACQI), a wrapper to manage the master SPI cores with two internal state machines, one dedicated to sending commands and the other for retrieving the sensing data. The ECPI interfaces each array segment with a dedicated SPI bus with four microcontrollers. In order to better comprehend the operation, the explanation of the two transmission processes is given in greater detail below.

Send Operation

The microcontrollers in the cluster array segment still run identical firmware to the previous version, except for the explained synchronization process. Consequently, the data packet structure remains unchanged, having fields for the function and value to receive.

The transmission initiates with the PS writing the registers *cmd_function* and *cmd_value* with the configuration data received from the host. Subsequently, the operation starts by setting the *cmd_send* bit, initiating the core internal process, a dedicated state machine in ACQI. This state machine manages the six master SPI cores, providing the correct sequencing of data, byte by byte, forming the data packet. This sequence repeats four times to address all the microcontrollers, six simultaneously. The operation ends after these sequences, resulting in the assertion of the *cmd_done* status bit. It ensures the delivery of the commands to all the microcontrollers, allowing the PS to resume operations.

Receive Data

In the receiving operation, the ECPI performs a demanding and complex task responsible for acquiring 480 bytes of data from the microcontrollers within the array segment cluster. The acquisition process state machine in ACQI starts or ends with the *acq_en* bit definition in the control register.

Upon initiation, data transfer begins in synchronization with a data-ready signal provided by one of the microcontrollers. This approach, similar to the one used in WECAP and represented in Figure 4.3.3, ensures that the normal sampling process of the array segments microcontrollers is not disturbed.

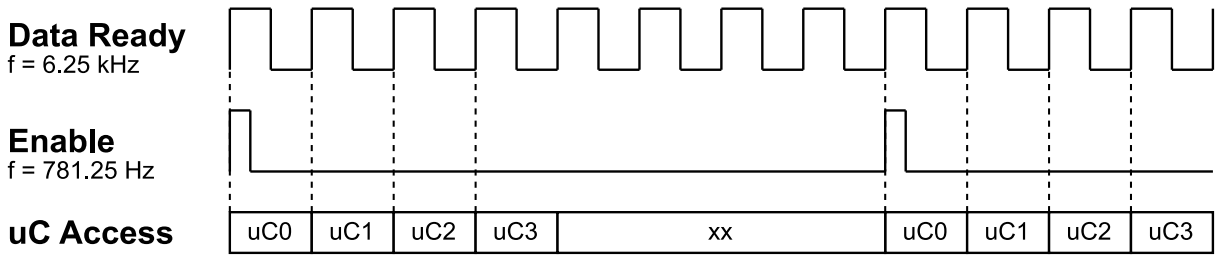

Figure 4.3.3: Generic time diagram example of ACQI data transfer.

In the diagram above, each data-ready rising edge triggers parallel data transfer from six microcontrollers, one of each array segment. This transfer occurs at a frequency of 781.85 Hz, changing according to the value set in the *dready_div* register following Equation (4.3.1).

$$f_{enable} = \frac{f_{data\_ready}}{4+dready\_div}. \quad (4.3.1)$$

As a result, the maximum enable-signal frequency achievable is 1.5625 kHz solving the WECAP latency issue. This frequency aligns with the 0.16 mm resolution goal for commercial PBF machines operating at 250 mm/s speed. The *dready_div* provides flexibility for slower setups, e.g., the CNC test assembly with a 160 mm/min speed requires setting the value to 371 to maintain the desired resolution. It is important to emphasize that the sampling frequency within the array segment cluster is much higher, operating at 31.125 kHz.

During the 120-byte transfer cycle, from six microcontrollers, the acquired data remains stored in a local array. After receiving all 480 bytes, the data is transferred to a local dual port, BRAM. This action triggers an interrupt from the IP core to the PS through the *irq* port, resulting in the PS initiating a DMA transfer. The AXI4-Stream Master design handles the BRAM addressing, enabling the data to shift through a dedicated bus in 64-bit packets. The data follows the path illustrated in Figure 4.3.2 until it reaches the external DDR3 memory. This process repeats as long as the *acq_en* bit is high.

4.3.4 Host Interface

The host interface represents the communication between an external computer running the LabView application and the StrixVision. Depending on the operation mode, this interface can use Bluetooth or ethernet. In compliance with the development roadmap, the device only supports the ethernet interface.

Concerning the ethernet development, the PL component is relatively straightforward, only requiring the peripheral configuration. The true challenge lies in the PS, the firmware development. Initially, the approach started with Petalinux [64], an embedded Linux development toolkit to enable ethernet functionality. However, it was unsuitable due to its significant overhead on the SoC resources.

Instead, the implementation relies on the most efficient approach, a bare-metal method using the Lightweight IP (LwIP), an open-source TCP/IP stack designed for embedded systems. It is suitable since it uses minimal resources while providing low latency and high throughput. The system behaves as a TCP server using a static IP address in the current configuration. In this design, the system waits for incoming TCP connections from the host to react accordingly.

In the typical operation sequence, the device enters an idle state on the power-up, waiting to establish a connection with the client (host computer) via the Ethernet cable. Afterward, the host system can open a TCP connection, allowing data exchange. The communication follows the data packet format used until now. This method allows the use of a similar interface process to the predecessor, which means handling the commands and the transference of the layers scan data follows the same concept.

4.4 Software

The application responsible for controlling and acquiring layer-wise scanning data remains consistent with the LabView for the WECAP version. Figure 4.4.1 shows the GUI interfacing with the StrixVision.

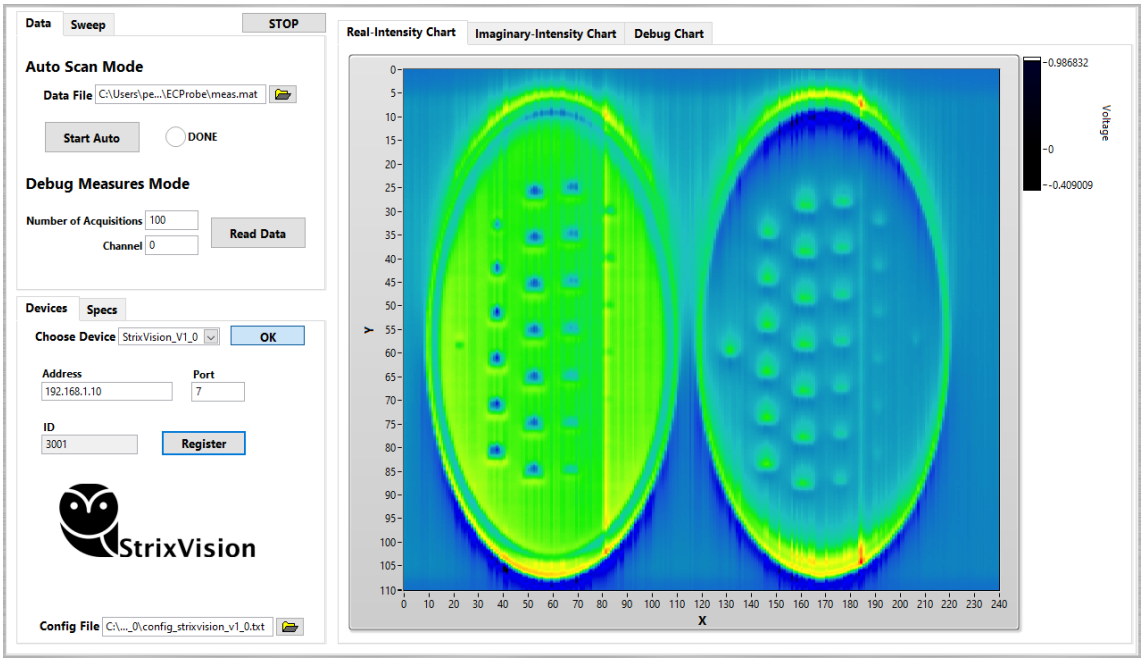

Figure 4.4.1: GUI to control the StrixVision and CNC.

Software development for StrixVision was minimal and straightforward. The existing software skeleton provides everything, requiring only the development of drivers for the new communication layer, resulting in a fast implementation. One noticeable change above is the Devices dynamic tab, which now displays the fields related to the ethernet connection instead of the previous COM ports.

The operation procedure, starting from the initial configuration and calibration measurements to initiating scan acquisitions, remains unchanged since using the same software structure. The main difference lies only in the backend in the data packets received from StrixVision, which now contain 512 bytes, with 480 valuable data from all the 240 channels within the device.

Currently, the StrixVision operates mounted on a CNC table with a single moving axis, the y-axis. The movement is continuous, achieving a 160 mm/min speed, resulting in a y resolution, as mentioned earlier, of 0.16 mm. The x-axis no longer incorporates a stepper to move to replicate the PBF operation conditions, resulting in a resolution of 1 mm determined by the sensing coils' pitch.

5. Results

5.1 Electromagnetic Geometry Simulations

The present section provides the stimulation and sensing electromagnetic geometries studies during the development of this project. It begins by providing the design choices and explanations behind the WECAP operation. The subsequent part discusses the StrixVision, focusing on an enhanced design to overcome limitations identified in the previous iteration.

5.1.1 WECAP

The WECAP development started by defining the stimulation and sensing topology. The prototype uses the reflection topology, where a single coil creates a uniform magnetic field, and sense coils monitor the EC. As stated in the background, the approach appears from the freedom to optimize the sensing and stimulation coils individually. Figure 5.1.1 illustrates the two designs developed.

The designs only differ in the number of turns of the stimulation coil. In principle, the design with more turns is better because the current flowing in each turn, with the same direction, adds up to a stronger magnetic field. The strengthened magnetic field induces larger eddy currents in the specimen, improving sensitivity. On the other hand, a higher number of turns also increases the coils' impedance, making it more challenging to drive. The other design appears in case the coil driver capabilities are insufficient.

Figure 5.1.1: Stimulation and Sensing design; (a) 1 turn, (b) 3 turns.

ANSYS Maxwell software was used to validate the magnetic field distribution within the two designs. It is a highly used and sophisticated Finite Element Analysis (FEA) simulation tool that facilitates defining the geometrical parameters, the material properties, and excitation conditions. The simulation verifies the magnetic field distribution and intensity levels in stainless steel with a sinusoidal 1 A stimulation at 1 MHz frequency, illustrated in Figure 5.1.2 (a) and Figure 5.1.2 (b).

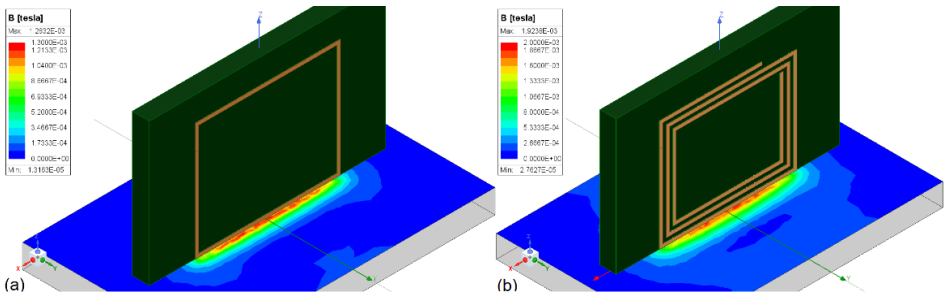

Figure 5.1.2: Material magnetic field distribution; 1 turn design (a), 3 turns design (b).

The previous images confirm a magnetic field concentration beneath the stimulation coil traces, displaying similar distributions. As anticipated, the three-turn coil configuration yields a significantly higher intensity magnetic field at the metal surface due to the tripled current passing closely over the material. WECAP adopts this configuration to enhance sensitivity but with the potential risk of a higher baseline signal. This strategic choice balances sensitivity and baseline considerations.

5.1.2 StrixVision

Before starting StrixVision development, the primary focus was refining the stimulation and sensing electromagnetic geometry design. The objective was to enhance the system sensitivity and spatial resolution. It is vital to recognize that spatial resolution is not solely dependent on the number of sensor elements in use; the stimulation and proximity to the material are equally critical, as elucidated in the upcoming explanations addressing two specific limitations contributing to the systems' performance.

The first challenge appears as a consequence of simplifying the AFE, resulting in a low dynamic range due to the absence of a reference coil to eliminate the baseline originated from the stimulation primary field. Consequently, this limits the maximum sensitivity achievable by the device. The studied solution involved placing the sensing coils parallel to the specimen under analysis. The stimulation coil would have several turns over the material, with current flowing in the same direction, canceling the primary magnetic field when placed in the air, replicating the reference coil concept. However, maintaining an effective intersection between the sensing coil winds and the secondary magnetic field (high flux linkage) required multilayer coils. The challenge appeared due to the market availability having only low inductance coils (2.7 µH), which is not a practical approach because of the low sensitivity.

The second limitation was detected when scanning PBF specimens using the WECAP version. While the results were decent in dense metal parts made with several negative structures (e.g., holes, voids), the device exhibited a significantly lower performance when detecting small metallic structures (e.g., lattices). Therefore, StrixVision presents a new design to enhance the results in such specimens, illustrated in Figure 5.1.3.

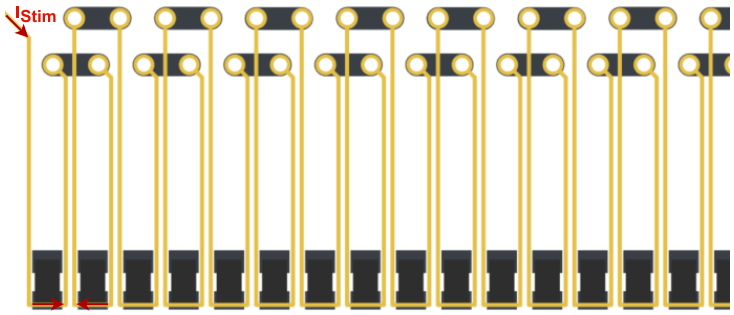

Figure 5.1.3: Enhanced Stimulation and Sensing design.

The low-quality results from the one-turn configuration coil result from its inability to induce enough eddy current loops in small metallic structures. Negative structure detection is a different scenario because the eddy current loops have a wide metallic area to close, generating a strong secondary magnetic field. The proposed solution uses the new stimulation coil design in Figure 5.1.3, with the coil path passing under the sensing coils and the current flowing in opposite directions. This design aims to increase the number of eddy current loops closing in the small metallic structures.

The design validation was carried out with ANSYS Maxwell simulations, considering a stainless-steel plate with an electrical conductivity of 1.1 MS/m. The stimulation uses a 1 A current flow at 1 MHz frequency. The first simulation, in Figure 5.1.4, analyzes the magnetic field distribution.

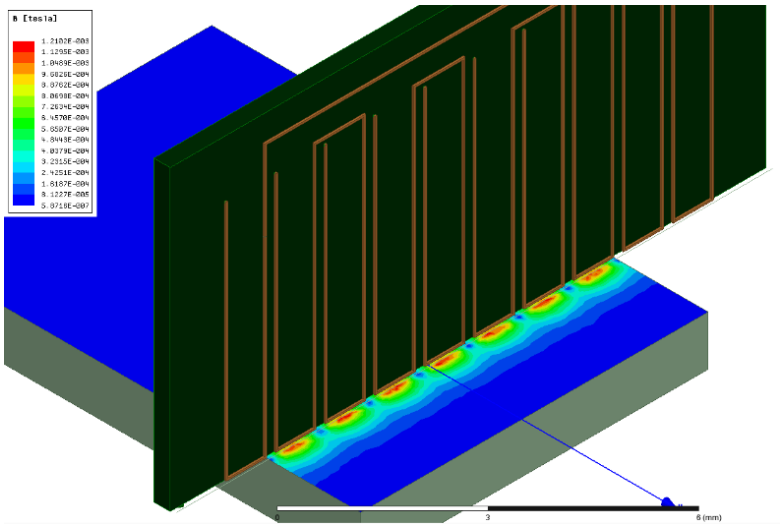

Figure 5.1.4: Material magnetic field distribution for the enhanced design.

The anticipated behavior is visible in the image above, with small localized magnetic fields under each sensing coil. The dedicated magnetic fields have equal magnitudes and opposite directions, creating null areas. The expectation is that the localized magnetic fields will help improve the spatial resolution by increasing the concentration of eddy currents in the small metallic structures.

The final simulations to validate the new design concept involves scanning two metal specimens, replicating both cases the WECAP was subjected to, a specimen with negative structure and a small positive structure, illustrated in Figure 5.1.5 (a) and (b) respectively. The structure in the specimens is a 2.5 mm diameter circle with 0.5 mm height.

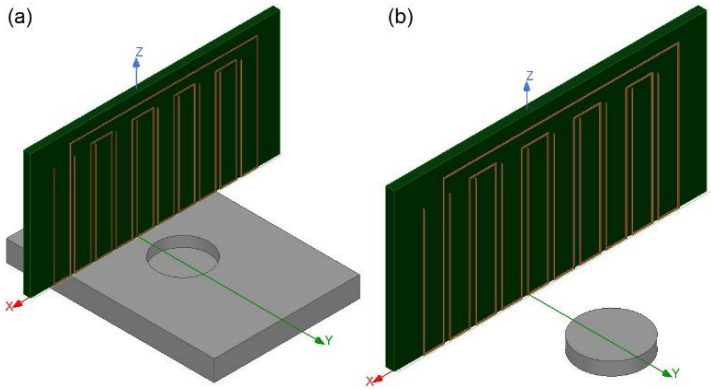

Figure 5.1.5: Simulation model using a negative structure (a) and positive structure (b)

The models' metal parts are still considered stainless steel plates and use the same stimulation characteristics. The following results, in Figure 5.1.6 and Figure 5.1.7, present the scan along the y-axis of the magnetics' field imaginary component at the height of the coils $Im\{B_Z\}$, for the positive and negative structures respectively. The images (a) and (c) use 0.01 mm x-axis resolution, the raw result from simulation with high-resolution. In order to emulate the sensing coil array view, the images (b) and (c) reflect a down-scaled image in the x-axis to a 1 mm pitch.

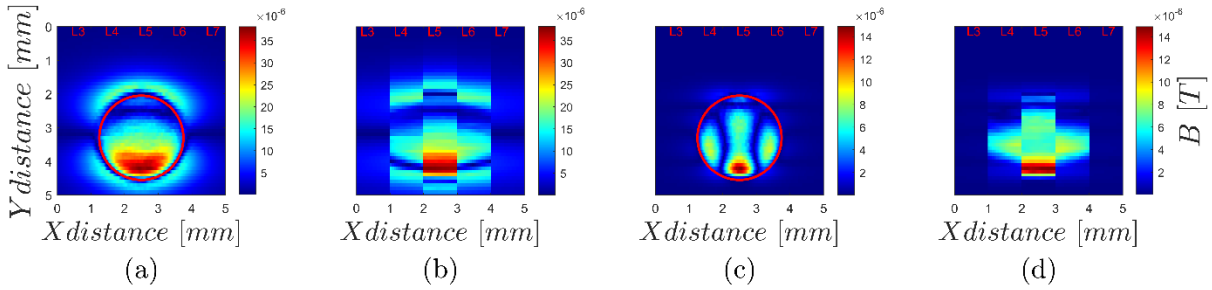

Figure 5.1.6: Positive structure magnetic field scan using (a) one-turn coil high-resolution, (b) one-turn low-resolution, (c) enhanced coil high-resolution, and (d) enhanced coil low-resolution.

The results are evident: the magnetic field distribution is higher over the specimen with the one-turn configuration coil, resembling a dipole distribution. In contrast, the enhanced coil provides a much more confined dispersion around the circle contour, indicating a higher resolution over the specimen. However, the sensing coils measure a field with intensity 2.5 times lower, resulting in a lower sensitivity, an effect of having a shorter coil length over the metallic structure.

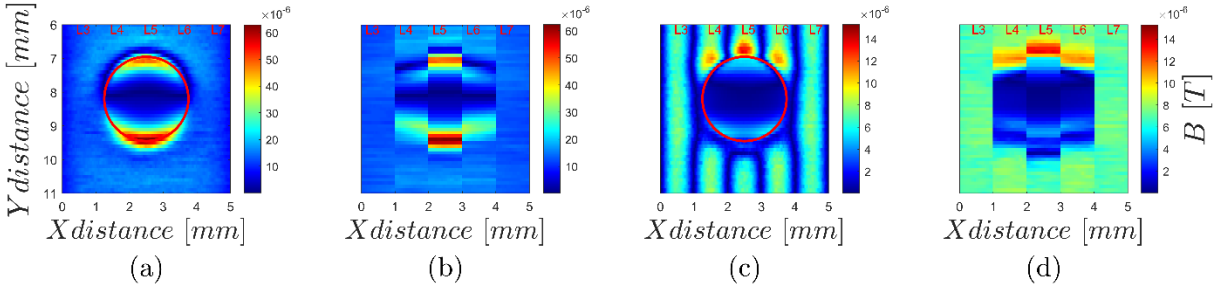

Figure 5.1.7: Negative structure magnetic field scan using (a) one-turn coil high-resolution, (b) one-turn low-resolution, (c) enhanced coil high-resolution, and (d) enhanced coil low-resolution.

Concerning the negative structure scan, it remains detectable with the enhanced design, but the resolution improvements are barely noticeable. An interesting observation, yet to be experimentally confirmed, is the invisibility of the null magnetic field in the sensing coils 2D reconstruction above. It happens because the design places the sensing coils in the middle of the localized fields. This phenomenon is also evident in the positive structure.

In summary, the new geometry design improves the results for small metallic structures. However, it is necessary to consider the tradeoff between sensitivity and resolution, especially for the negative structures. The experimental evaluation is going to dictate the optimal choice for the equipment. However, the enhanced design, although promising, remains untested due to the complex design, making it highly resistive, with an overall value of 68 Ω. The StrixVision still uses the standard one-wire configuration, but in the future, with the newer SCM operating, it will be tested to validate the concept.

5.2 Measurement Setup

Access to a real PBF machine is challenging, particularly in Portugal, where only a handful of companies might have. Negotiating an agreement to assemble the StrixVision on such expensive equipment is complex. Instead, the measurement setup, illustrated in Figure 5.2.1, emulates the L-PBF setup. The StrixVision mounts on a CNC (1) using a custom PVC fixture (2). The specimens (3) are placed on a wood base, enabling scan speeds up to 160 mm/min. The laptop (4), running the developed LabView application (5), handles the control, data acquisition, and the 2D image reconstruction.

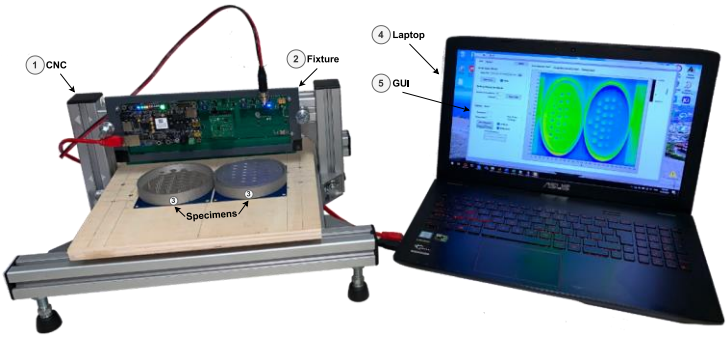

Figure 5.2.1: StrixVision measurement setup.

In this chapter, several results are presented and discussed using the measurement setup above. The discussion initiates with the evaluation of the equipment through generic PCB scans, followed by a detailed analysis of scans conducted on LB-PBF-produced specimens. Notice that WECAP results are not analyzed since the overall device design is identical, producing similar results.

5.3 Preliminary

After testing the equipment, the first step is to perform scans over 100x100 mm sample PCBs with distinct patterns. It is essential to assess what requires fine-tuning, such as stimulation current amplitude and MAF number of samples, and to verify the actual imaging reconstruction outcome. The PCBs' dark regions correspond to the Flame Retardant 4 (FR4) material and brighter areas to 0.35 µmm copper.

The first scan is a simple circle pattern with an outer diameter of 25 mm and an inner of 15 mm (5 mm thickness), illustrated in Figure 5.3.1 (a) with the amplitude imaging results in Figure 5.3.1 (a) and (b).

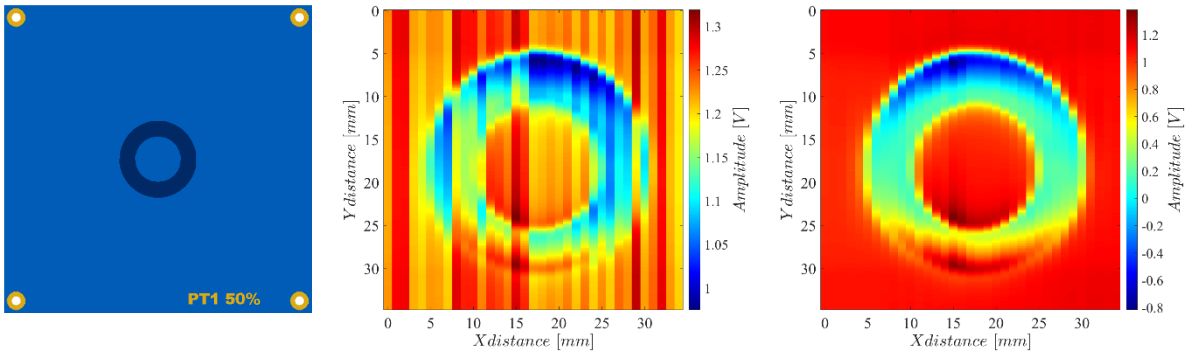

(a) (b) (c)

Figure 5.3.1: Circle pattern (a), imaging result without compensation (b), and final imaging (c).

The imaging result in Figure 5.3.1 (b) presents a significant mismatch among all the channels. The most evident reason is the channels' AFE differences, especially having 1% tolerance components defining the gain and the bias point, which could explain part of the problem. Second, the amplifier output impedance mismatches and the ADC sample and hold capacitor dispersion also contribute. However, the source is mainly from the coils' lift-off and orientation, which even with automated assembly is inevitable. Fortunately, there is a solution, and it is possible to improve the raw image and obtain the result in Figure 5.3.1 (c). The method to enhance the data consists of performing a simple data processing under LabView before showing the final reconstruction, following

$$result = \frac{raw_{scan} - c_{air}}{c_{metal} - c_{air}}. \tag{5.3.1}$$

where raw_{scan} is the scan measurement matrix, c_{air}, and c_{metal} are calibration measures obtained before initializing the scan with the probe placed on the air and over the metal, respectively. The Equation aims to compensate the raw_{scan} measurements for sensitivity and offset mismatches. In the numerator, subtracting c_{air} from the raw_{scan} allows removing the effects of lift-off. The division by $c_{metal} - c_{air}$ normalizes the data, ensuring the numerator falls into the expected range between metal and air, improving the sensitivity and the offset mismatches among all the channels.

Scanning with the StrixVision, covering a 240 mm length array, allowed the same scan pass to include two additional patterns. The first pattern is a 25x25 mm squared frame with a 5 mm width in Figure 5.3.2 (a), while the second concerns a QR code pattern with a more complex design in Figure 5.3.2 (c).

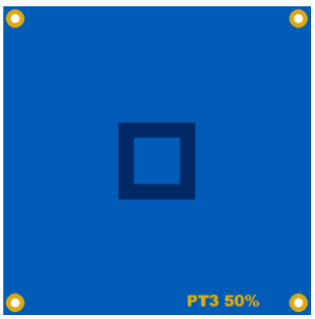

(a)

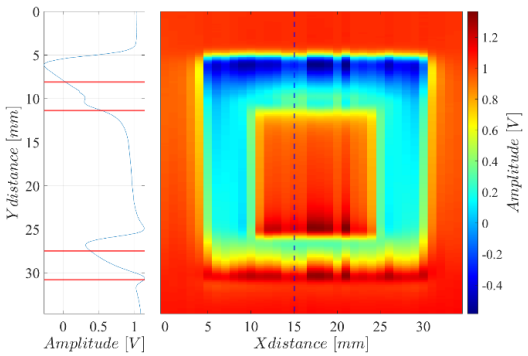

(b)

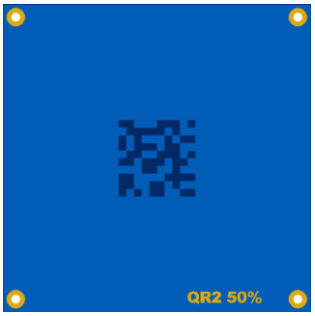

(c)

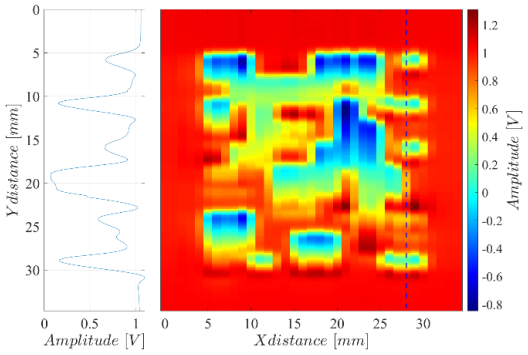

(d)

Figure 5.3.2: Frame pattern (a), frame imaging (b), QR code pattern (c), QR code imaging (d).

Considering the scan travel direction, the squared frame result in Figure 5.3.2 (b) shows an early increase of the magnetic field in the transitions from FR4 to copper. These regions are marked in red in the auxiliary voltage graph transient at the 15 mm x-axis position. The phenomenon is a legacy issue resulting from the physical offset between the stimulation coil and the sensing line. Although StrixVision reduced the offset, the effect persists. This effect arises because, during the transitions, the stimulation coil moves in front of the sensing line. Consequently, the sensing line starts picking up a stronger magnetic field sooner as the stimulation approaches the copper first.

In Figure 5.3.2 (c), the reconstruction of the QR code demonstrates that even when scanning complex metallic designs, the pattern remains recognizable but contains the offset issue more often. There are two possible solutions to overcome the issue. The first is software compensation to counteract the early increases. The second approach consists of scanning each layer twice but requires probe rotation. The problem would manifest symmetrically, allowing the two images to overlap, potentially improving the overall result. However, some LB-PBF recoaters only pass over the specimen once to distribute the metal powder. An alternative could involve aligning the stimulation coil with the sensing coils, besides being discarded in 5.1.1, it might be worth exploring in future tests to address the problem effectively.

5.4 LB-PBF Specimens Imaging

The final validation test for StrixVisions' capabilities consists of one-layer imaging on two-dimensional scans over LB-PBF-produced parts. These samples, manufactured using SS316 powder in a RenAM 500S Flex LB-PBF machine present in Instituto de Soldadura e Qualidade (ISQ), were designed to emulate two variants of what an additive-manufactured part can be. Part one, illustrated in Figure 5.4.1, is a high-density metal with negative structures, while part 2, in opposition, features positive metal structures depicted in Figure 5.4.1 (b).

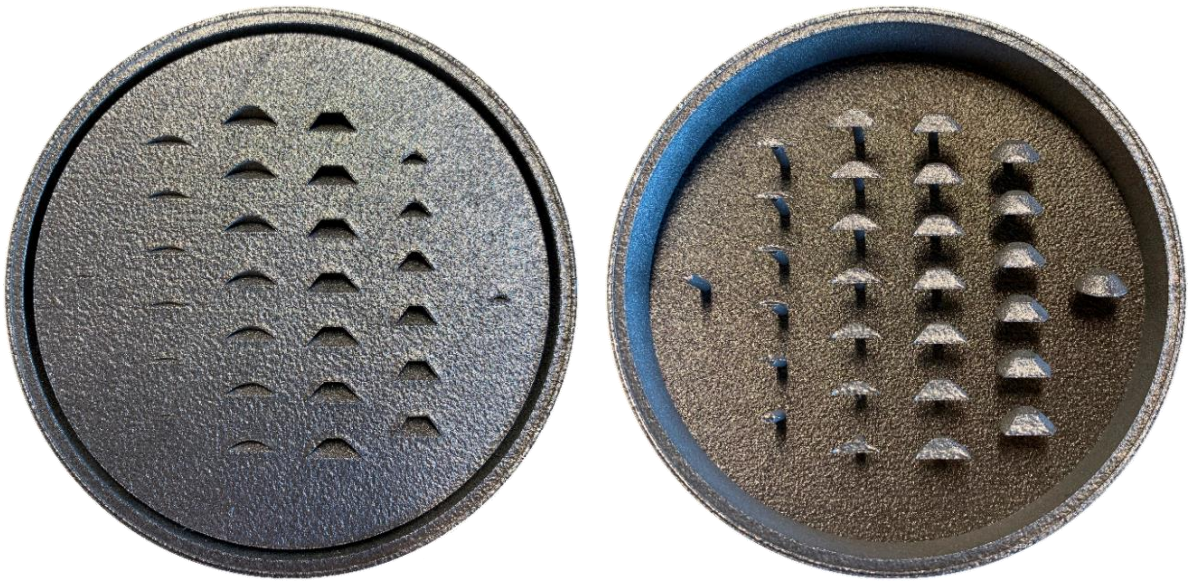

(a) (b)

Figure 5.4.1: Top view of the LB-PBF produced part 1 (a) and part 2 (b).

The specimens are designed with a frustum cone placed at different heights to create negative and positive structures. This design enables the evaluation of the probe with different superficial sizes and depths. The scanning area in the right image is an inversion of the negative part.

The probe setup includes a total lift-off of around 0.4 mm, with 0.3 mm attributed to the circular parts frame and 0.1 mm to prevent the probe from scratching the metal. In a real scenario, it would be reduced to 0.1 mm, providing higher sensitivity, but the probe still features a raw voltage variation between air and metal around 104 mV. As stated in 4.2.1, the stimulation coil driving current is 700 mA peak to peak. The combined length of both parts side-by-side is 206 mm, requiring a single pass to obtain both results.

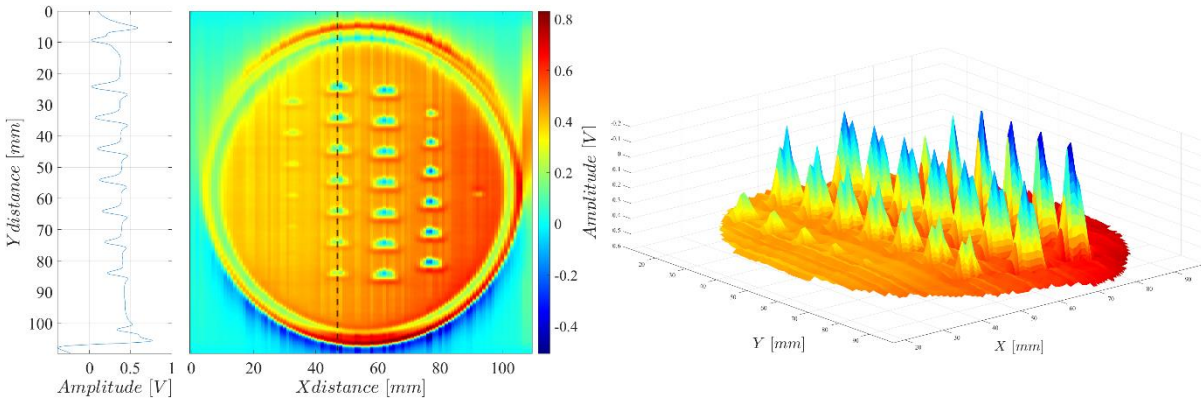

Figure 5.4.2: Amplitude imaging result on a two-dimensional scan over the LB-PBF part 1.

The imaging results for part one, in Figure 5.4.2, accurately reconstruct the metal part, capturing variations in the superficial size corresponding to the structures. Additionally, it is possible to verify an apparent decrease in amplitude with the increase of the y-axis, which relates to the decrease in depth of the structures. Despite the channels mismatch over the metal, the variation in value is low compared to the structures' detection. Due to the decent SNR, the mismatch is neglectable in the reconstruction.

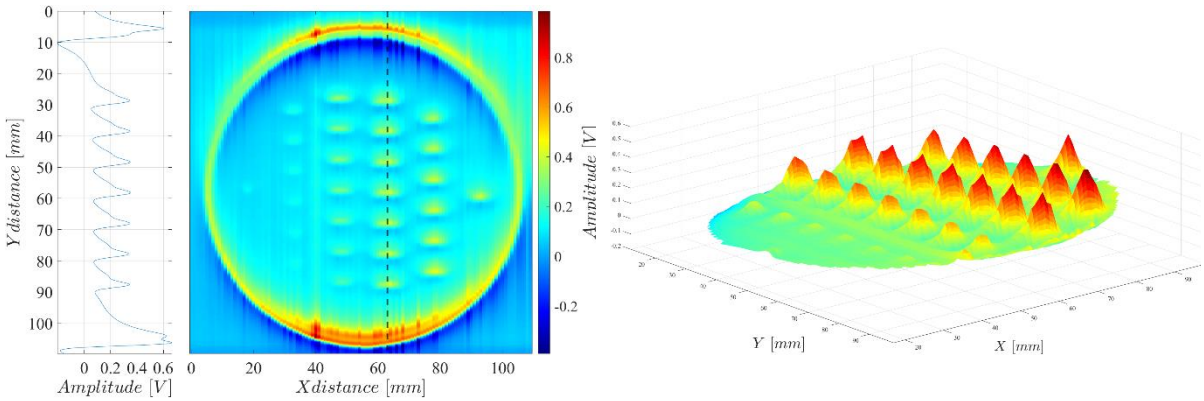

Figure 5.4.3: Amplitude imaging result on a two-dimensional scan over the LB-PBF part 2.

The imaging result for metal part two, in Figure 5.4.3 is decent, showing higher intensity in the superficial metal and a fadeout effect representing the depth of the structures. However, there is a decrease in sensitivity over the metal structures compared to the previous negative structures. It confirms the statements in 5.1.2 about the lack of spatial resolution over the specimens.

The results above do not include the powder due to the post-cleaning process. However, the electrical conductivity of the powder is significantly lower than the consolidated material, not affecting the results [61]. In summary, the results align with the expectations for the StrixVision design. Retrieving data from the 240 channels in parallel with a 0.16 mm resolution along the y-axis is possible. However, the x-axis resolution must improve to characterize the smaller structures, either negative or positive.

6. Conclusions

This work presents the development process of a new ECP array to scan PBF-produced parts layer-by-layer. Achieving the objectives demanded a deep dive into several domains, the electromagnetism fundamentals, and the architecture and design of a mixed signals embedded system.

WECAP is a development platform for studying, modeling, and validating the new concept, aiming for a high-frequency readout probe with enhanced spatial resolution. This new probe presents an optimized approach for acquiring material integrity data. Starting with the AFE, with remarkably low complexity compared to the traditional methods, leads to a small form factor and improves the spatial resolution. Additionally, it attenuates channel mismatch and minimizes temperature dependencies. Second, the SCM provides a method to drive coils with a current achieving 700 mA peak-to-peak effectively and generate a strong magnetic field. Lastly, the high-speed digital core, together with all the optimizations, provides 0.48 mm scan resolution without slowing down the PBF recoater.

The WECAP development led to the creation of a versatile wireless demo kit that is battery-powered and makes scanning PBF parts effortless. Besides operating as a demonstrator, the system holds great potential to integrate an AM machine to prove the concept. Efforts are underway to validate the layer-wise imaging capabilities in the RenAM 500S Flex LB-PBF machine of ISQ. The plans are to monitor an entire specimen production, marking a significant step towards the industry.

The final iteration, the StrixVision, was developed to fulfill the scalability objective, extending the scan length from 40 mm to an impressive 240 mm. The implementation aligns multiple enhanced WECAP designs and incorporates a powerful SoC to retrieve and transmit all scanning data to a host system. The SoC integration brings flexibility to the probe, leaving the addition of features open. The system exhibited an outstanding performance that was aligned with the objectives, decreasing the scan resolution to 0.16 mm, with the only drawback being the lack of time preventing further development.

The current design successfully demonstrated the probes' imaging capabilities and ability to reconstruct the PBF specimens. However, it also exhibited a lack of resolution along the sensing line axis, a limitation resulting from the stimulation and sensing electromagnetic geometry. The inferior performance was clear from the beginning. It is important to remember that the simulations using an enhanced stimulation coil present encouraging results to overcome the spatial resolution limitations. However, the focus on improving the physical spatial resolution down to 1 mm and accommodating a significant number of channels to cover the PBF powder bed was achieved.

This thesis ends up providing a complete ECP array device. Nonetheless, there is work remaining to fulfill the industry requirements. Below is listed the future work recognized as crucial:

- Continue the StrixVision missing features development: the wireless functionality and the position sensor (e.g., optical) to obtain the produced layers' start and finish positions.
- Validate the probes' layer-wise imaging performance in a real PBF machine.
- Improve the sensing and stimulation electromagnetic geometry. Improving the stimulation spatial resolution, attenuating the primary magnetic field baseline, and eliminating the offset problem are vital for enhancing the imaging results.
- Study the possibility of using lower-size package coils or replacing the sensing sensors with MR to decrease the spatial resolution to better characterize the small structures on the specimens.

References

[1] C. Zhao *et al.*, “Real-time monitoring of laser powder bed fusion process using high-speed X-ray imaging and diffraction,” *Sci Rep*, vol. 7, no. 1, Dec. 2017, doi: 10.1038/s41598-017-03761-2.

[2] “Standard, Standard Tterminology for Additive Manufacturing Technologies,” *ASTM Standard F2792-12a*. ASTM International, 2012. doi: 10.1520/F2792-12A.

[3] S. Everton, P. Dickens, and C. J. Tuck, “IDENTIFICATION OF SUB-SURFACE DEFECTS IN PARTS PRODUCED BY ADDITIVE MANUFACTURING, USING LASER GENERATED ULTRASOUND Moisture Transport Through pores in porous asphalt pavement View project Additive Manufacturing and Electric Motors View project.” [Online]. Available: https://www.researchgate.net/publication/330926198

[4] J. M. Waller and σ Nasa-Jsc Wstf, “Nondestructive Testing of Additive Manufactured Metal Parts Used in Aerospace Applications,” 2018. [Online]. Available: https://ntrs.nasa.gov/search.jsp?R=20180001858

[5] L. W. Koester, H. Taheri, T. A. Bigelow, and P. C. Collins, “Nondestructive Testing for Metal Parts Fabricated Using Powder-Based Additive Manufacturing.” [Online]. Available: https://www.researchgate.net/publication/324209458

[6] “EMLAYERING - ElectroMagnetic LAYER-wise testING for powder bed fusion metal additive manufacturing.” Accessed: Oct. 18, 2023. [Online]. Available: https://www.it.pt/AutomaticPage?id=3486

[7] S. Chowdhury *et al.*, “Laser powder bed fusion: a state-of-the-art review of the technology, materials, properties & defects, and numerical modelling,” *Journal of Materials Research and Technology*, vol. 20, pp. 2109–2172, Sep. 2022, doi: 10.1016/j.jmrt.2022.07.121.

[8] J. García-Martín, J. Gómez-Gil, and E. Vázquez-Sánchez, “Non-destructive techniques based on eddy current testing,” *Sensors*, vol. 11, no. 3. pp. 2525–2565, Mar. 2011. doi: 10.3390/s110302525.

[9] G. Developers, “Ampere-Maxwell.” Accessed: Oct. 09, 2022. [Online]. Available: https://em.geosci.xyz/content/maxwell1_fundamentals/formative_laws/ampere_maxwell.html?highlight=ampere%20law

[10] G. Developers, “Faraday’s Law.” Accessed: Oct. 09, 2022. [Online]. Available: https://em.geosci.xyz/content/maxwell1_fundamentals/formative_laws/faraday.html

[11] L. S. Rosado, “New eddy current probes and digital signal processing algorithms for friction stir welding testing , PhD. dissertation, Instituto Superior Técnico,” 2014. doi: 10.13140/RG.2.2.11657.36962.

[12] H. M. G. Ramos, O. Postolache, F. C. Alegria, and A. L. Ribeiro, “Using the skin effect to estimate cracks depths in structures,” in *2009 IEEE Intrumentation and Measurement Technology Conference, I2MTC 2009*, IEEE Computer Society, 2009, pp. 1361–1366. doi: 10.1109/IMTC.2009.5168668.

[13] NDE-Ed.org, “Complex Impedance Plane: Eddy Current Scope.” Accessed: Oct. 23, 2022. [Online]. Available: https://www.nde-ed.org/NDETechniques/EddyCurrent/Instrumentation/impedanceplane.xhtml

[14] “Introduction to Eddy Current Testing.” Accessed: Oct. 23, 2022. [Online]. Available: https://www.olympus-ims.com/en/ndt-tutorials/eca-tutorial/intro/

[15] “Detecting Corrosion in Aluminum with Eddy Current Array Technology.” Accessed: Oct. 23, 2022. [Online]. Available: https://www.eddyfi.com/en/appnote/detecting-corrosion-in-aluminum-with-eddy-current-array-technology

[16] NDE-Ed.org, “Eddy Current Standards and Methods.” Accessed: Oct. 25, 2022. [Online]. Available: https://www.nde-ed.org/NDETechniques/EddyCurrent/ET_Tables/standardsmethods.xhtml

[17] British Institute of Non-Destructive Testing, “Eddy Current Testing (ET),” NDT-related standards - Eddy Current Testing (ET). Accessed: Oct. 25, 2022. [Online]. Available: https://www.bindt.org/international-and-european-standards/ndt-related-standards/eddy-current-testing/

[18] ISO, “DIN EN ISO 15548-1,” *Part 1: Instrument characteristics and verification*. International Organization for Standardization (ISO), 2009.

[19] ISO, “DIN EN ISO 15548-2,” *Part 2: Probe characteristics and verification*. International Organization for Standardization, 2003.

[20] ISO, “DIN EN ISO 15548-3,” *Part 3: System characteristics and verification*. International Organization for Standardization (ISO), 2004.

[21] EOS, “Additive Manufacturing for Space Propulsion.” Accessed: Nov. 01, 2022. [Online]. Available: https://www.eos.info/en/all-3d-printing-applications/aerospace-3d-printing/space-propulsion-satellites

[22] D. Systèmes, “3D Printing - Additive.” Accessed: Oct. 31, 2022. [Online]. Available: https://make.3dexperience.3ds.com/processes/powder-bed-fusion

[23] M. E. H. Ehlers, “Development of a High-Spatial Resolution Eddy Current Testing Array for Online Process Monitoring of Additively Manufactured Parts, MSc. Thesis, Technischen Universität Berlin,” 2023. doi: 10.14279/depositonce-17572.

[24] C. Cavallo, “All About Powder Bed Fusion 3D Printing.” Accessed: Oct. 31, 2022. [Online]. Available: https://www.thomasnet.com/articles/custom-manufacturing-fabricating/powder-bed-fusion-3d-printing/

[25] D. D. Gu, W. Meiners, K. Wissenbach, and R. Poprawe, “Laser additive manufacturing of metallic components: materials, processes and mechanisms,” *International Materials Reviews*, vol. 57, no. 3, pp. 133–164, May 2012, doi: 10.1179/1743280411Y.0000000014.

[26] T. D. Ngo, A. Kashani, G. Imbalzano, K. T. Q. Nguyen, and D. Hui, “Additive manufacturing (3D printing): A review of materials, methods, applications and challenges,” *Compos B Eng*, vol. 143, pp. 172–196, Jun. 2018, doi: 10.1016/j.compositesb.2018.02.012.

[27] S. M. Yusuf, S. Cutler, and N. Gao, “The impact of metal additive manufacturing on the aerospace industry,” *Metals (Basel)*, vol. 9, no. 12, Dec. 2019, doi: 10.3390/met9121286.

[28] P. Ahangar, M. E. Cooke, M. H. Weber, and D. H. Rosenzweig, “Current biomedical applications of 3D printing and additive manufacturing,” *Applied Sciences (Switzerland)*, vol. 9, no. 8, Apr. 2019, doi: 10.3390/app9081713.

[29] F. Calignano, M. Galati, and L. Iuliano, “A metal powder bed fusion process in industry: Qualification Considerations,” *Machines*, vol. 7, no. 4, 2019, doi: 10.3390/machines7040072.

[30] M. Grasso and B. M. Colosimo, “Process defects and in situ monitoring methods in metal powder bed fusion: A review,” *Meas Sci Technol*, vol. 28, no. 4, Apr. 2017, doi: 10.1088/1361-6501/aa5c4f.

[31] J. P. M. Pragana *et al.*, “Influence of processing parameters on the density of 316L stainless steel parts manufactured through laser powder bed fusion,” *Proc Inst Mech Eng B J Eng Manuf*, vol. 234, no. 9, pp. 1246–1257, Jul. 2020, doi: 10.1177/0954405420911768.

[32] S. Clijsters, T. Craeghs, S. Buls, K. Kempen, and J. P. Kruth, “In situ quality control of the selective laser melting process using a high-speed, real-time melt pool monitoring system,” *International Journal of Advanced Manufacturing Technology*, vol. 75, no. 5–8, pp. 1089–1101, Oct. 2014, doi: 10.1007/s00170-014-6214-8.

[33] T. G. Fleming, S. G. L. Nestor, T. R. Allen, M. A. Boukhaled, N. J. Smith, and J. M. Fraser, “Tracking and controlling the morphology evolution of 3D powder-bed fusion in situ using inline coherent imaging,” *Addit Manuf*, vol. 32, Mar. 2020, doi: 10.1016/j.addma.2019.100978.

[34] J. L. Bartlett, F. M. Heim, Y. v. Murty, and X. Li, “In situ defect detection in selective laser melting via full-field infrared thermography,” *Addit Manuf*, vol. 24, pp. 595–605, Dec. 2018, doi: 10.1016/j.addma.2018.10.045.

[35] G. Mohr *et al.*, “In-situ defect detection in laser powder bed fusion by using thermography and optical tomography—comparison to computed tomography,” *Metals (Basel)*, vol. 10, no. 1, Jan. 2020, doi: 10.3390/met10010103.

[36] M. Kalms, R. Narita, C. Thomy, F. Vollertsen, and R. B. Bergmann, “New approach to evaluate 3D laser printed parts in powder bed fusion-based additive manufacturing in-line within closed space,” *Addit Manuf*, vol. 26, pp. 161–165, Mar. 2019, doi: 10.1016/j.addma.2019.01.011.

[37] R. J. Smith, M. Hirsch, R. Patel, W. Li, A. T. Clare, and S. D. Sharples, “Spatially resolved acoustic spectroscopy for selective laser melting,” *J Mater Process Technol*, vol. 236, pp. 93–102, Oct. 2016, doi: 10.1016/j.jmatprotec.2016.05.005.

[38] D. Pieris *et al.*, “Laser Induced Phased Arrays (LIPA) to detect nested features in additively manufactured components,” *Mater Des*, vol. 187, Feb. 2020, doi: 10.1016/j.matdes.2019.108412.

[39] J. P. Oliveira, T. G. Santos, and R. M. Miranda, “Revisiting fundamental welding concepts to improve additive manufacturing: From theory to practice,” *Prog Mater Sci*, vol. 107, Jan. 2020, doi: 10.1016/j.pmatsci.2019.100590.

[40] A. A. Martin *et al.*, “Dynamics of pore formation during laser powder bed fusion additive manufacturing,” *Nat Commun*, vol. 10, no. 1, Dec. 2019, doi: 10.1038/s41467-019-10009-2.

[41] B. Sasi, A. V, C. K. Mukhopadhyay, and R. B.P.C., “Enhanced detection of deep seated flaws in 316 stainless steel plates using integrated EC-GMR sensor,” *Sens Actuators A Phys*, vol. 275, pp. 44–50, Jun. 2018, doi: 10.1016/j.sna.2018.03.040.

[42] M. A. Machado, K. N. Antin, L. S. Rosado, P. Vilaça, and T. G. Santos, “Contactless high-speed eddy current inspection of unidirectional carbon fiber reinforced polymer,” *Compos B Eng*, vol. 168, pp. 226–235, Jul. 2019, doi: 10.1016/j.compositesb.2018.12.021.

[43] A. Sophian, G. Tian, and M. Fan, “Pulsed Eddy Current Non-destructive Testing and Evaluation: A Review,” *Chinese Journal of Mechanical Engineering (English Edition)*, vol. 30, no. 3. Chinese Mechanical Engineering Society, pp. 500–514, May 01, 2017. doi: 10.1007/s10033-017-0122-4.

[44] A. S. Repelianto, N. Kasai, K. Sekino, and M. Matsunaga, “A uniform eddy current probe with a double-excitation coil for flaw detection on aluminium plates,” *Metals (Basel)*, vol. 9, no. 10, Oct. 2019, doi: 10.3390/met9101116.

[45] M. A. Machado, L. S. Rosado, N. M. Mendes, R. M. Miranda, and T. G. Santos, “Multisensor inspection of laser-brazed joints in the automotive industry,” *Sensors*, vol. 21, no. 21, Nov. 2021, doi: 10.3390/s21217335.

[46] A. S. Repelianto, N. Kasai, K. Sekino, M. Matsunaga, and L. Q. Trung, “Flaw detection in aluminum plates using a rotating uniform eddy current probe with two pairs of excitation coils,” *Metals (Basel)*, vol. 9, no. 10, Oct. 2019, doi: 10.3390/met9101069.

[47] L. S. Rosado, T. G. Santos, P. M. Ramos, P. Vilaça, and M. Piedade, “A new dual driver planar eddy current probe with dynamically controlled induction pattern,” *NDT and E International*, vol. 70, pp. 29–37, 2015, doi: 10.1016/j.ndteint.2014.09.009.

[48] M. A. Machado, L. S. Rosado, and T. G. Santos, “Shaping Eddy Currents for Non-Destructive Testing Using Additive Manufactured Magnetic Substrates,” *J Nondestr Eval*, vol. 41, no. 3, Sep. 2022, doi: 10.1007/s10921-022-00882-1.

[49] C. Mandache, “Overview of non-destructive evaluation techniques for metal-based additive manufacturing,” *Materials Science and Technology (United Kingdom)*, vol. 35, no. 9, pp. 1007–1015, Jun. 2019, doi: 10.1080/02670836.2019.1596370.

[50] M. A. Spurek *et al.*, “Relative density measurement of pbf-manufactured 316l and alsi10mg samples via eddy current testing,” *Metals (Basel)*, vol. 11, no. 9, Sep. 2021, doi: 10.3390/met11091376.

[51] A. Spierings *et al.*, “ETH Library Direct part density inspection in laser powder bed fusion using eddy current testing Conference Paper,” Sep. 2021, doi: 10.3929/ethz-b-000516133.

[52] M. A. Spurek *et al.*, “In-situ monitoring of powder bed fusion of metals using eddy current testing,” *Addit Manuf*, p. 103259, Nov. 2022, doi: 10.1016/j.addma.2022.103259.

[53] W. Zhang, C. Wang, F. Xie, and H. Zhang, “Defect imaging curved surface based on flexible eddy current array sensor,” *Measurement (Lond)*, vol. 151, Feb. 2020, doi: 10.1016/j.measurement.2019.107280.

[54] E. I. Todorov, P. Boulware, and K. Gaah, “Demonstration of array eddy current technology for real-time monitoring of laser powder bed fusion additive manufacturing process,” SPIE-Intl Soc Optical Eng, Mar. 2018, p. 40. doi: 10.1117/12.2297511.

[55] H. Ehlers, M. Pelkner, and R. Thewes, “Heterodyne Eddy Current Testing Using Magnetoresistive Sensors for Additive Manufacturing Purposes,” *IEEE Sens J*, vol. 20, no. 11, pp. 5793–5800, Jun. 2020, doi: 10.1109/JSEN.2020.2973547.

[56] L. S. Rosado, P. M. Ramos, and M. Piedade, “Real-time processing of multifrequency eddy currents testing signals: Design, implementation, and evaluation,” *IEEE Trans Instrum Meas*, vol. 63, no. 5, pp. 1262–1271, 2014, doi: 10.1109/TIM.2013.2283633.

[57] D. M. Caetano *et al.*, “High-Resolution Nondestructive Test Probes Based on Magnetoresistive Sensors,” *IEEE Transactions on Industrial Electronics*, vol. 66, no. 9, pp. 7326–7337, Sep. 2019, doi: 10.1109/TIE.2018.2879306.

[58] D. M. Caetano, M. Piedade, J. Fernandes, T. Costa, J. Graça, and L. Rosado, “A CMOS ASIC for Precise Reading of a Magnetoresistive Sensor Array for NDT.”

[59] H. Ehlers, M. Pelkner, and R. Thewes, “Online Process Monitoring for Additive Manufacturing Using Eddy Current Testing With Magnetoresistive Sensor Arrays,” *IEEE Sens J*, vol. 22, no. 20, pp. 19293–19300, Oct. 2022, doi: 10.1109/JSEN.2022.3205177.

[60] A. Barrancos Oliveira, “Eddy Current Array Probe for Metal Additive Manufacturing Imaging, MSc. Thesis, Instituto Superior Técnico,” 2021.

[61] A. Barrancos, R. L. Batalha, and L. S. Rosado, “Towards Enhanced Eddy Current Testing Array Probes Scalability for Powder Bed Fusion Layer-Wise Imaging,” *Sensors*, vol. 23, no. 5, Mar. 2023, doi: 10.3390/s23052711.

[62] “AN118 - Improving ADC Resolution by Oversampling and averaging,” Jul. 2013.

[63] “AVR121: Enhancing ADC resolution by oversampling Features.”

[64] “PetaLinux Tools.” Accessed: Nov. 28, 2023. [Online]. Available: https://www.xilinx.com/products/design-tools/embedded-software/petalinux-sdk.html